FINAL TECHNICAL REPORT
FOR
HIGH-SPEED, LONG-WAVELENGTH COHERENT
RADIATION DETECTORS

R. L. Williams

Texas Instruments Incorporated

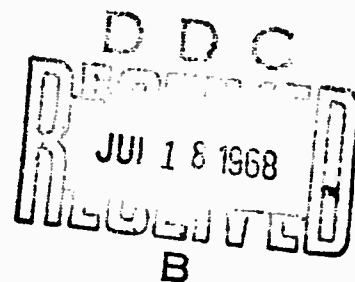15 May 1967 Through 14 May 1968

Contract N00014-67-C-0497

63

FINAL TECHNICAL REPORT
FOR
HIGH-SPEED, LONG-WAVELENGTH COHERENT
RADIATION DETECTORS

R. L. Williams

Texas Instruments Incorporated

ABSTRACT

The four major sections of this report are concerned with four main areas of research performed under Contract N00014-67-C-0497. The first section deals with the appearance of dielectric relaxation time constant components. These arise when the drift length of holes becomes comparable to the electrode separation, so that a significant fraction of the photogenerated holes is swept from the crystal. Under these conditions, which correspond to having the photoconductive gain of the order of or greater than unity, there is a maximum D^* bandwidth product. The second section is concerned with the D^* bandwidth calculation and also points up the superiority of p-i-n diode performance over that of photoconductors if speed in excess of 10^{-9} second is required at 10.6 microns.

In the third section gettering and contact effects are reported. It is shown that a gallium diffused layer getters copper from Ge:Hg. Using radioactive copper, we have demonstrated a very irregular distribution of copper in the vicinity of the diffusion profile. In addition, photovoltaic studies have revealed an expected potential distribution near the contact.

Some general considerations on heterodyne detection form the fourth section of the report. Serious inefficiencies arise with misalignment of the local oscillator beam on an intrinsic photoconductor. A collinear mode of operation is shown to eliminate this effect, and studies of transparent contacts are reported. Finally, the loss of signal for misalignment of local oscillator and signal beams has been calculated for a variety of detector sizes and 10.6 micron radiation.

iii

TABLE OF CONTENTS

TABLE OF CONTENTS
continued

LIST OF ILLUSTRATIONS

LIST OF ILLUSTRATIONS

continued

LIST OF TABLES

BLANK PAGE

SECTION I

RESPONSE CHARACTERISTICS OF EXTRINSIC PHOTOCONDUCTORS

A. Introduction

When mercury- and copper-doped germanium photoconductors are operated in the helium-hydrogen temperature range, their resistances are determined by the photon flux of the environment. For flux densities low enough for the material resistivity to be a megohm-cm or greater the speed of response of the photoconductor is limited to the dielectric relaxation response time τ_ρ. This parameter is determined by the resisitivity ρ and the dielectric constant ϵ of the photoconductor and through the relationship

$$\tau_\rho = \epsilon \epsilon_o \rho \tag{1}$$

(ϵ_o is the permitivity of free space).

The earliest report of dielectric relaxation effects in extrinsic germanium materials is in the noise measurements by Klaassen, et al.[1] A later theoretical article presented a noise analysis which included dielectric relaxation terms.[2] This theory involved arbitrary coefficients for the amplitude of the dielectric relaxation noise terms, but pointed up the fact that noise components with frequency terms dependent on τ_ρ should be observed.

In an article by Williams[3] the dielectric relaxation response time was identified in mercury-doped germanium photoconductors. At that time, speculation on the origin of the dielectric relaxation phenomena centered on non-uniformities of the crystal. It has been established now that nonuniformities are not necessary for the effect to be present; rather, the phenomena originate from sweepout of the charge carriers.

B. Theory

In this subsection we will present data that demonstrate that the readjustment time τ_ρ is observed for a given resistivity only if the drift length of carriers

1

is comparable to or greater than the electrode separation. Space charge and dielectric relaxation effects are to be expected when photogenerated charge is being swept out of the crystal [Figure 1(a)].

Consider a photoconductor in equilibrium with a particular photon flux incident on the detector. Dependent on the carrier lifetime, there is a hole carrier concentration p_0 and an ionized impurity concentration N_{Hg}^- mercury atoms/cc in Ge:Hg. The resistivity of the material is then $(\mu_p p_0 q)^{-1}$, where μ_p is the hole mobility and q the electronic charge.

The dielectric response characteristic is easiest to visualize by considering the response to a delta function light pulse. In a time shorter than all the other time periods of interest this pulse of radiation produces a carrier concentration increase of Δp and an increase in the ionized impurity concentration of ΔN_{Hg}^-, where $\Delta N_{Hg}^- \equiv \Delta p$. For a situation in which the carrier lifetime is long compared to the transit time, the Δp holes are swept out of the crystal, leaving the excess ionized impurity behind. This net charge is distributed uniformly through the crystal, as depicted in Figure 1(a), along with the steady state concentrations N_{Hg}^- and p_0.

The excess ionized impurity concentration ΔN_{Hg}^- gives rise to a nonuniform field component ΔE, depicted in Figure 1(b). The magnitude of ΔE is calculated by solving Poisson's equation

$$\frac{dE}{dx} = - \varepsilon \varepsilon_0 \, q \, \Delta N_{Hg}^- \qquad . \tag{2}$$

Solving this equation to include the unperturbed field $E_0 = V/L$, we obtain

$$E = - \varepsilon \varepsilon_0 \, q \, \Delta N_{Hg}^- \, (L - x) - V/L \qquad . \tag{3}$$

This perturbation to the steady field, $\Delta E = - \varepsilon \varepsilon_0 \, q \, \Delta N_{Hg}^- (L - x)$, is the restoring force returning the crystal to a charge neutrality situation.

2
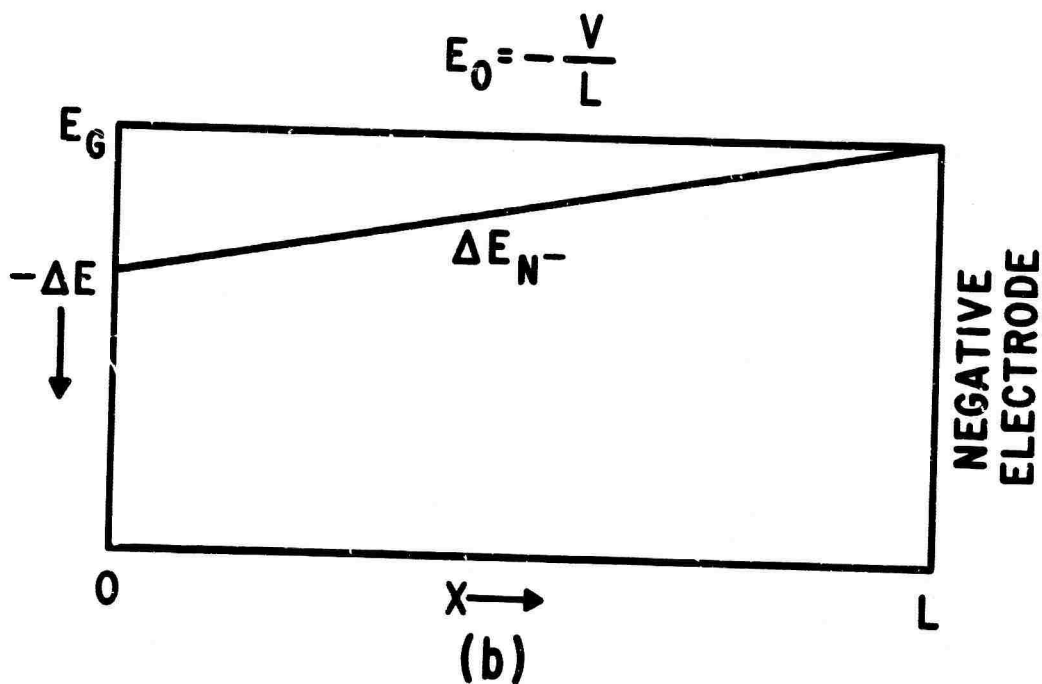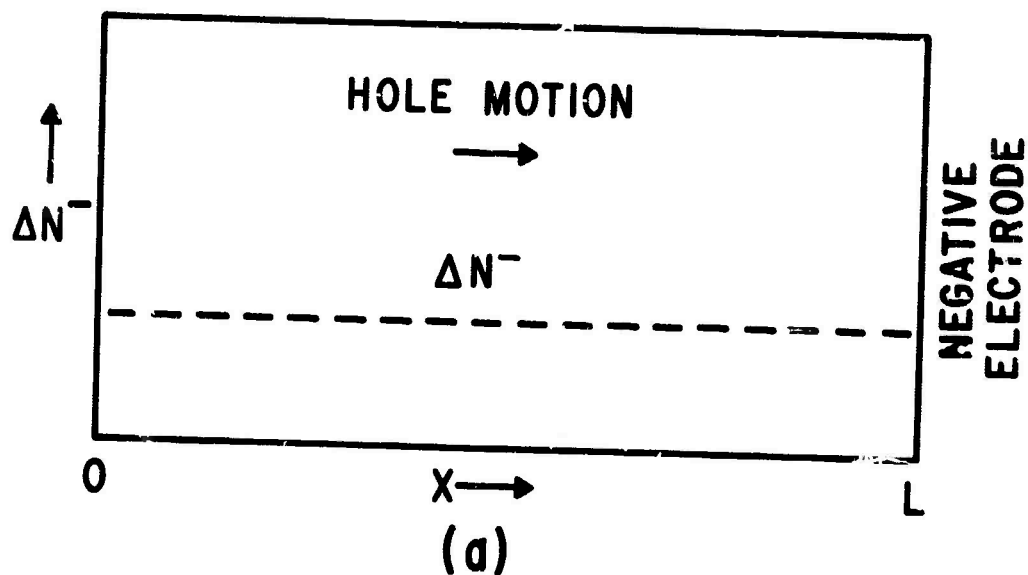
Figure 1 Space Charge Resulting from Sweepout. (a) Holes swept out of an extrinsic photoconductor leave behind excess charged impurity centers. (b) This space charge perturbs the electric field; a uniform charge distribution produces a linear perturbing field. Neutralization of this space charge takes place in a dielectric relaxation time.

2425-8

3

If we neglect generation and recombination, the continuity equation takes the form

$$\frac{d\Delta N_{Hg}^-}{dt} = \frac{1}{q}\frac{dJ_x}{dx} \qquad . \qquad (4)$$

In this equation J is the current density in the x direction and is given by

$$J = \mu_p \, q \, p_o \, E \qquad . \qquad (5)$$

Since only E is assumed to vary, substituting Equation (5) in (4) leads to

$$\frac{d\Delta N_{Hg}^-}{dt} = \mu_p p_o \, dE/dx \qquad , \qquad (6)$$

which by Equation (2) gives

$$\frac{d\Delta N_{Hg}^-}{dt} = - \frac{\mu_p p_o}{\epsilon\epsilon_o} q \, \Delta N_{Hg}^- \qquad . \qquad (7)$$

The solution to (7) in terms of the initial net charge concentration $\Delta N_{Hg}^-(o)$ is

$$\Delta N_{Hg}^-(t) = \Delta N_{Hg}^-(o) \exp - t/\tau_\rho \qquad , \qquad (8)$$

where $\tau_\rho = \dfrac{\epsilon\epsilon_o}{\mu_p p_o q} = \epsilon\epsilon_o \rho_o \qquad . \qquad (9)$

Thus the excess charge ΔN_{Hg}^- decays toward zero with a dielectric relaxation time constant τ_ρ.

To capitulate, space charge is created in the bulk of the semiconductor because mobile charge is swept out of the sample. The time required for the

4

crystal to neutralize the space charge depends on the resistivity of the material. Further, if the steady state field is low so that only a small fraction of the photogenerated charge is swept out of the crystal, only a small portion of the crystal will have a non-zero net charge.

The factor which determines the extent of the space charge is the drift length S of the carriers. The distance the holes are transported in a field E is determined by the hole mobility μ_p, and the time before recombination τ_ℓ, namely

$$S = \mu_p \, \tau_\ell E \qquad . \tag{10}$$

The role of drift distance can be visualized by referring to Figure 2. Considering again the response to a short pulse of light, we find that the holes move a distance S in the electric field, and those within a distance S of the negative electrode are swept out of the crystal. However, the ionized mercury atoms in the region of the negative electrode are neutralized by holes moving into this region from the bulk of the crystal. The sweepout of holes at the negative electrode, accompanying the drift of all the holes a distance S, produces a region of space charge at the positive electrode. This space charge region, S wide, is neutralized in a time τ_ρ.

C. Experimental

1. General

Most of the experiments for this contract were performed under variable flux environment in a radiation-tight chamber. The radiation flux within the enclosure was determined by the direct current through an InAs light emitting diode. Speed of response measurements were performed utilizing a second InAs diode in the pulse mode. Details of the arrangement are given in Reference 3. The carrier mobility-lifetime product was evaluated by using a calibrated blackbody source and calculating the number of absorbed photons using the known spectral response of the photoconductor. Samples had electrode areas of 1 mm x 5 mm and interelectrode separations of 0.33, 1.0, and 3.0 mm. In every

5

HOLE MOTION

SPACE
CHARGE
REGION

NEGATIVE
ELECTRODE

EXTRINSIC PHOTOCONDUCTOR

$$S = \mu E \tau$$

5158-10

S

L
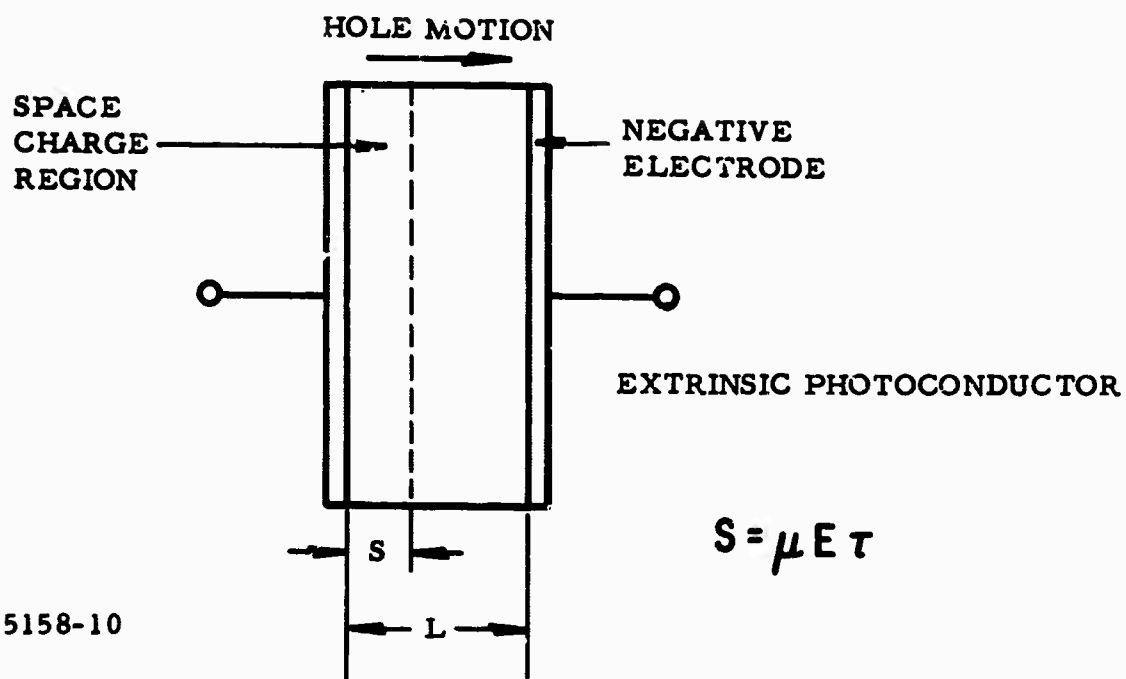
Figure 2   Space Charge Region and Drift Length. When the drift length S of
holes is less than the electrode separation, the space charge
region is S wide. As the drift length increases with increasing
electric field, the transient space charge region grows to encompass
the whole crystal.

6

experiment at least four elements were mounted on a sample holder, and the data obtained from all four units were very similar.

Since we found that resistivity rather than temperature determines the dielectric relaxation effects, the data to be presented were taken near helium temperatures. Results were the same when measurements were performed at higher temperatures.

2. Response Time Measurements

The fundamental result of the study was the observation of a long time constant response component when the bias on the detectors was increased. Figures 3 and 4 show oscillographs taken under small and large signal conditions. In both cases as the bias voltage is increased, a long time constant component appears which dominates the signal above a certain bias level.

The differences in the form of the response curves of Figures 3 and 4 depend on the magnitude of the resistance change due to the signal ΔR compared to the steady state resistance value R.

The rise and decay have essentially the same form for $\Delta R/R < 0.3$ (Figure 3) but are distinctively different for $\Delta R \gg R$ (Figure 4). In the large signal case of Figure 4 the leading portion of the signal, which is the "light-on" part of the response, has a distinct fast and slow component, while the decay has a complex characteristic since the resistance is changing as the decay progresses. Because the fast and slow components of the turn-on are more readily distinguished in the large signal case, most of the data were taken using the large signal response. Using the value of the resistivity of the detector material corresponding to that with the radiation signal on, we obtained good agreement between the measured response time and the calculated dielectric relaxation time constant. (In both Figures 3 and 4 the "radiation on" corresponds to the rising portion of the signal.)

The oscillographs were analyzed by determining the fast component A_f and the slow component A_ρ of the signal. The ratio A_ρ/A_f was then plotted as a

7

BIAS VOLTS

45
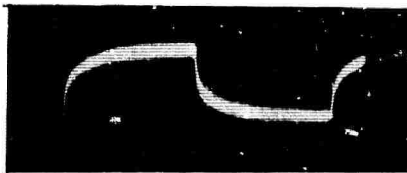
30
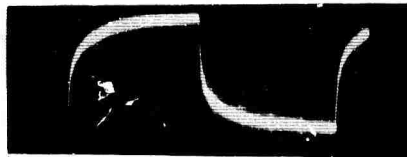
15
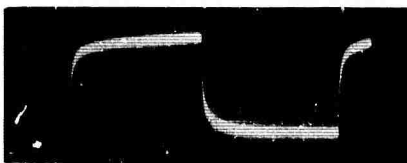
8

4
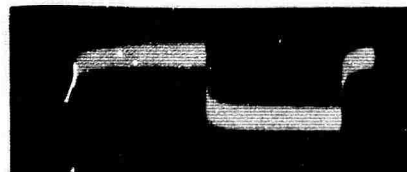
2
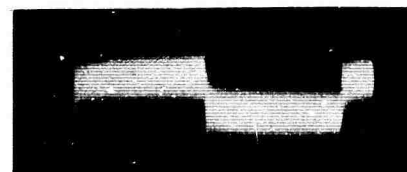
5425-10

Figure 3   Growth of the Dielectric Relaxation Component with Bias, ΔR/R
Small. With increasing bias a slow component of the signal appears.
With ΔR/R small the rise and decay are essentially the same. Electrode
separation was 3 mm, sweep speed 20 μsec/cm, and resistivity
30 MΩ-cm. The number to the left of the oscillograph picture is the
detector bias. Helium operating temperatures.

8

45 V   10 μsec/cm

23 V   10 μsec/cm

I 2 V   10 μsec/cm

6 V   5 μsec/cm

I.5 V   5 μsec/cm

5158-10
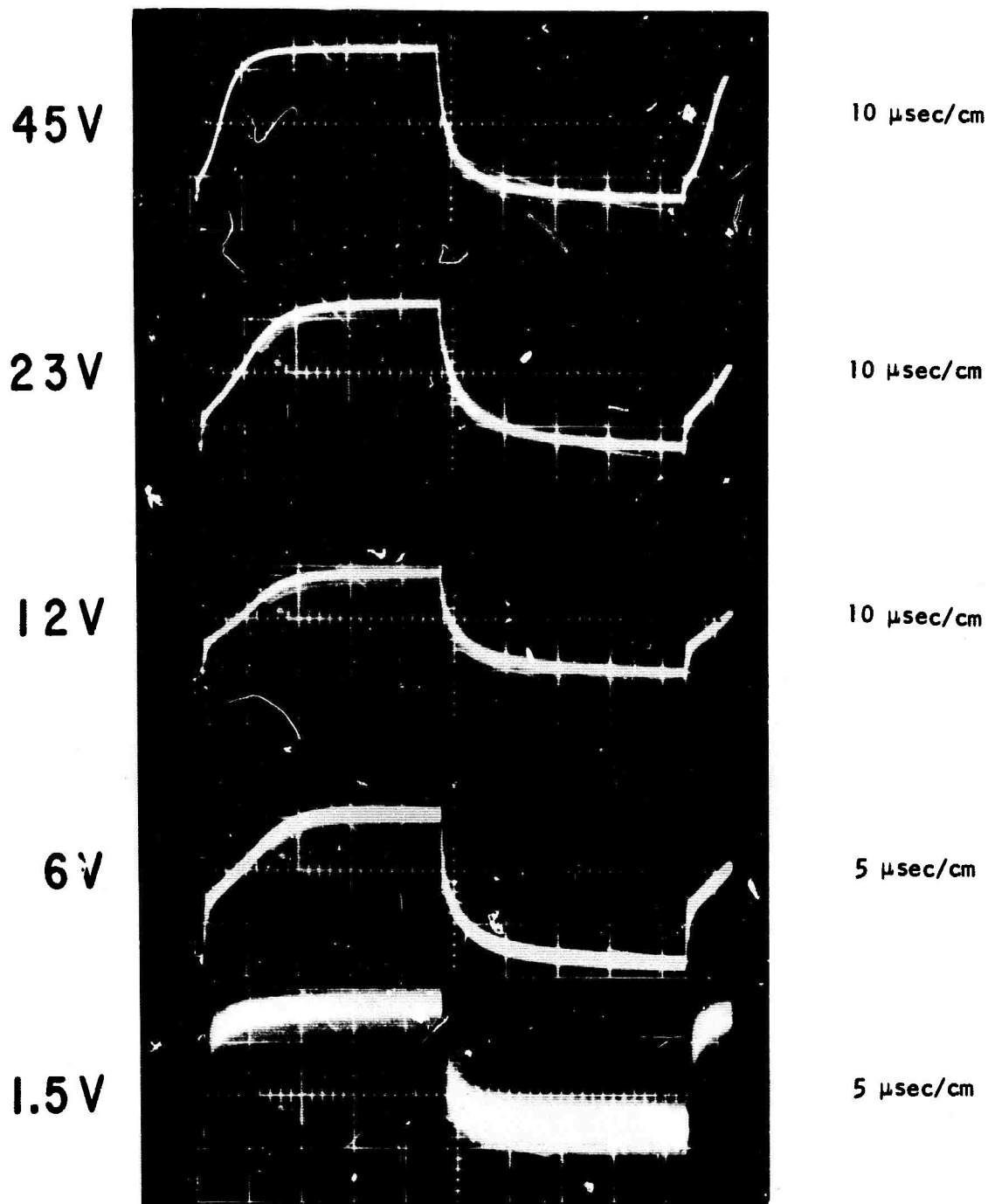
Figure 4 Growth of the Dielectric Relaxation Component with Electric Field, ΔR/R Large. With increasing bias the slow component of the signal dominates. For the large ΔR/R case the rise has a distinct break in the curve separating the fast and slow components while the decay has a complex form. The number to the left of the oscillograph picture is the detector bias; the number to the right is the sweep speed. Detector resistivity was 8 MΩ-cm and electrode separation 1.0 mm.

9

function of electric field. Figures 5, 6, and 7 contain such data from a variety of experimental conditions. Figure 5 contains data from crystals having a range of sensitivities and different contacting techniques. By each curve are the crystal number and the calculated mobility-lifetime product determined from photosensitivity.

The principal feature to note is that the field required to reach the point $A_p/A_f = 1$ (E_p) increases as the $\mu\tau$ product of the material decreases. Further, the curves labelled "end" and "top" are curves for samples mounted so that the signal radiation was incident through the end of the sample (i.e., parallel to the contact) and through the top of the sample (i.e., perpendicular to the contact). This top and end study was carried out to establish that the direction of the incident radiation played no part in the dielectric relaxation phenomena.

Three contacting procedures were used: indium solder or gold-gallium alloys on mercury-doped germanium and gallium diffused layers or indium solder on copper-doped germanium. With these various contacting techniques the onset of the dielectric relaxation effects correlated with material sensitivity.

Charge removal from a crystal depends not only on the carrier lifetime or drift distance but also on the distance the charge must travel to reach a contact, as illustrated by the data plotted in Figure 6. These data were taken with many of the same materials used for Figure 5, but electrode separation was 0.33 mm instead of 1.0 mm. This smaller spacing allowed all the materials tested to be biased to a value high enough so that the drift length became longer than the electrode spacing. Again, E_p increases as $\mu_p \tau_\ell$ decreases.

The dependence of E_p on electrode separation is most clearly illustrated in Figure 7. All data for crystal 1170 were taken with the same material. The successive sets of data, from 3.0 to 1.0 to 0.33 mm, were obtained by recutting and grinding the 3 mm starting element. It is clear that E_p varies in proportion to the sample thickness.
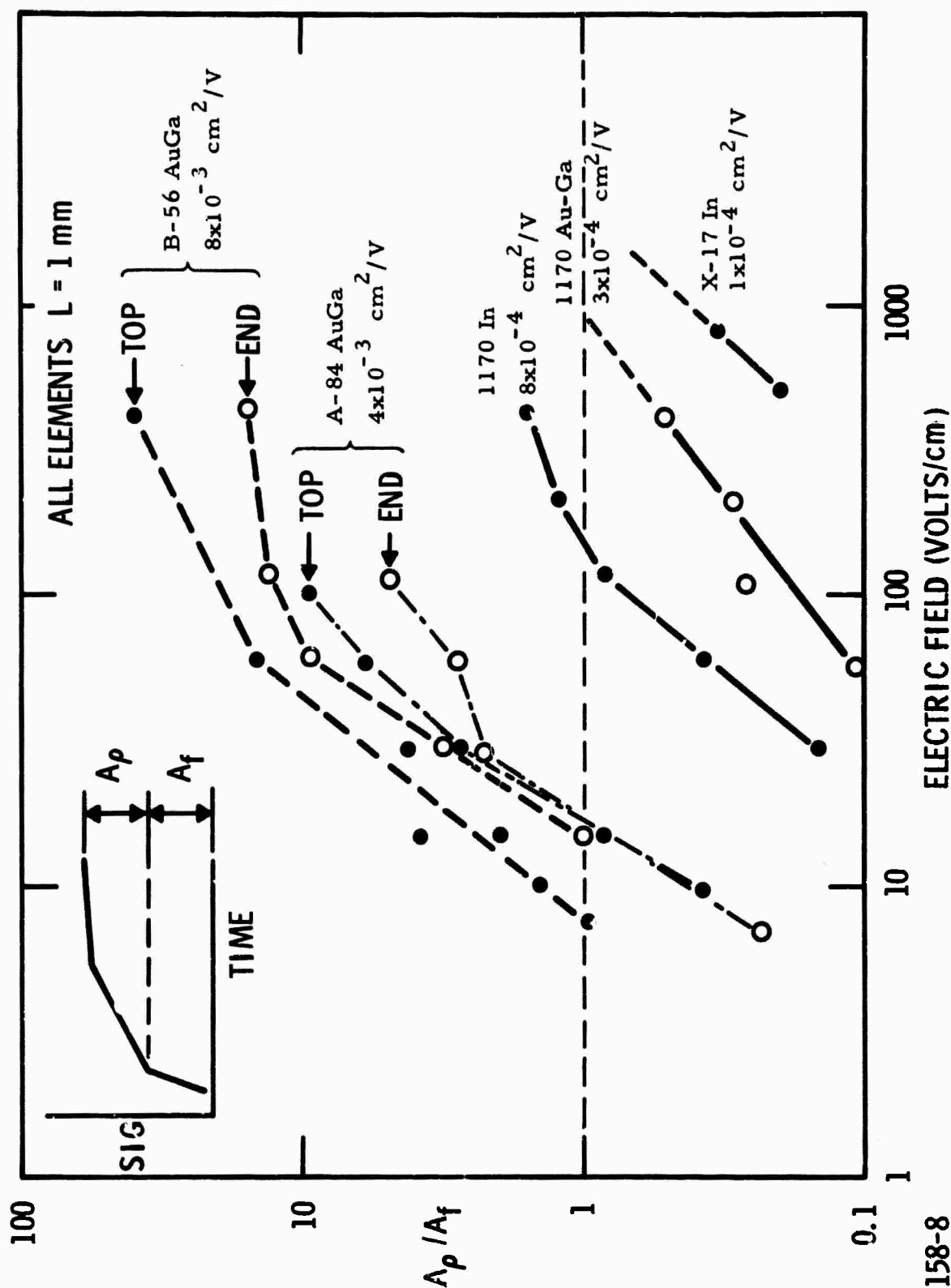
Figure 5 Variation of A_p/A_f (see insert) with Electric Field for Detector Materials with Various Mobility-Lifetime Products - L = 1 mm. With smaller $\mu\tau$ products higher electric fields are required to obtain $A_p/A_f = 1$. Radiation incident through the contacts (top) produces results similar to those with radiation incident on the end of the sample.

5158-8

11

5425-2
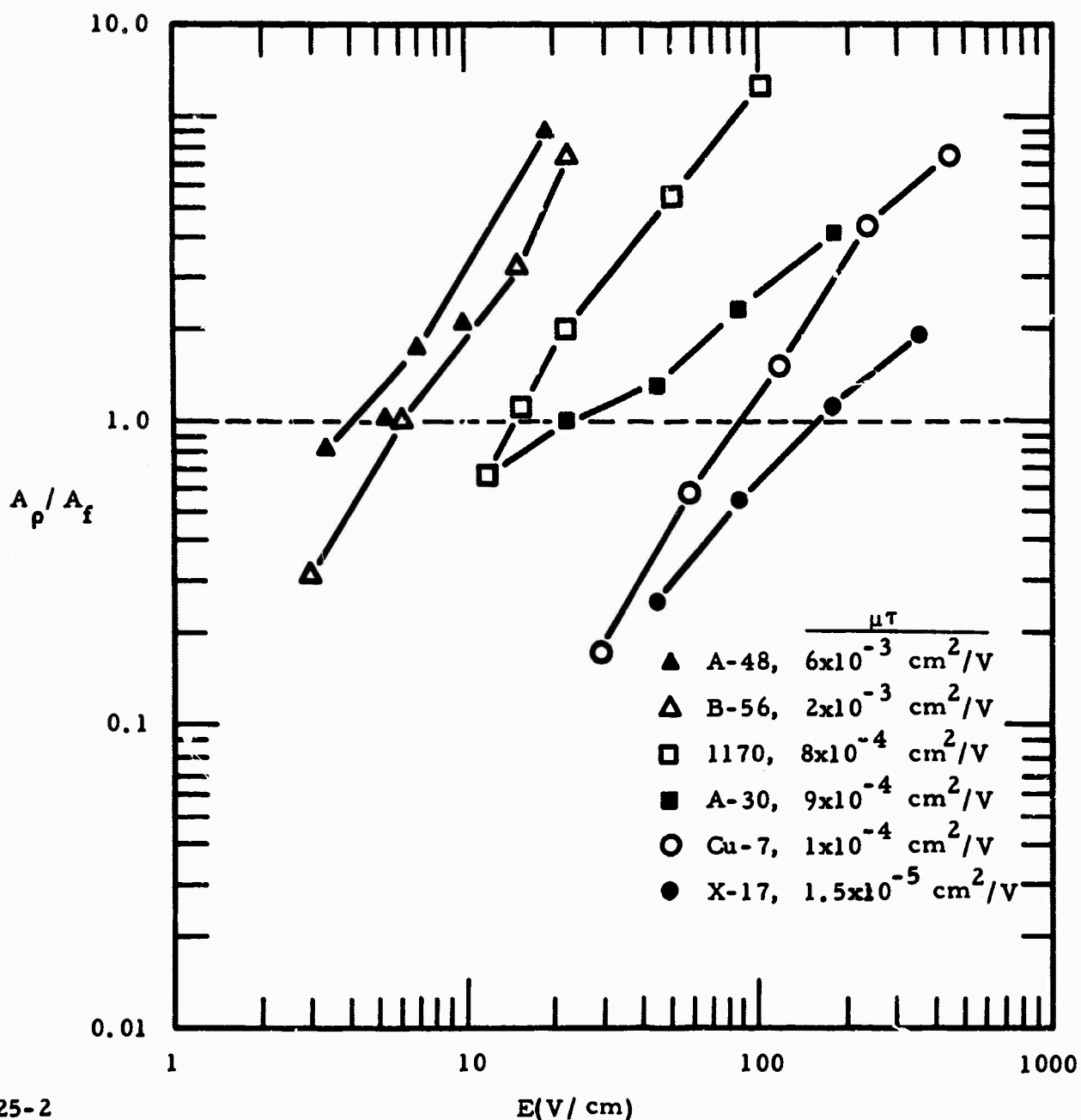
Figure 6   Variation of A_ρ/A_f with Electric Field for Detector Materials with Various Mobility-Lifetime Products - L = 0.33 mm. For thinner elements the A_ρ/A_f = 1 point is reached with smaller electric fields, since the holes must drift a shorter distance. Again, the field for 50% dielectric relaxation response increases as the $\mu\tau$ product decreases.

12
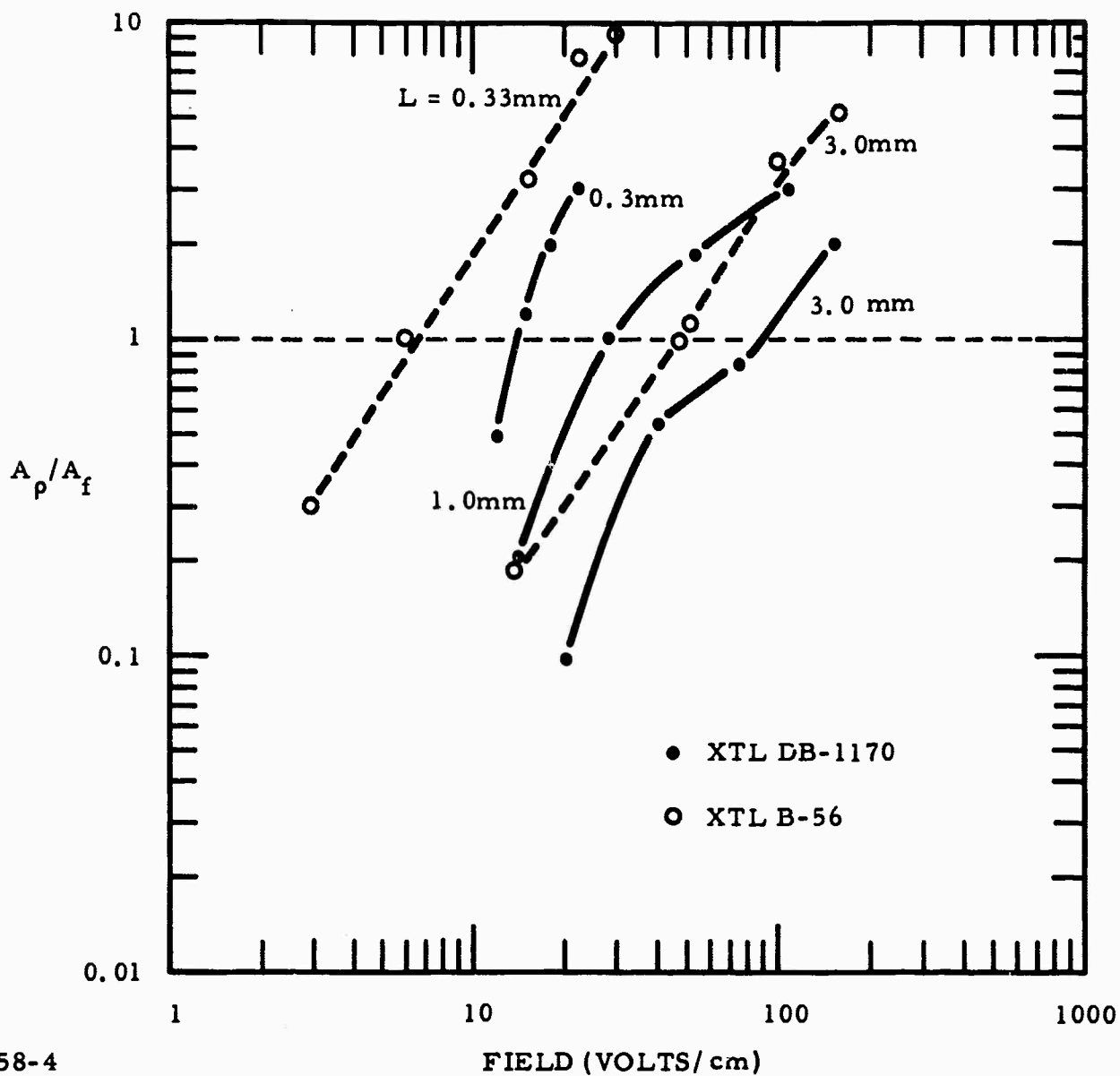
Figure 7 Variation of Field Dependence of A_ρ/A_f with Electrode Separation. When the same samples, No. 1170, are reprocessed to produce 3.0, 1.0, and 0.33 mm elements, the $A_\rho/A_f = 1$ point electric field is found to vary in proportion to the electrode separation. The same variation is found for crystal B-56 for samples cut from the same or adjacent wafers.

5158-4

13

The second set of data in Figure 7, taken only with 0.33 and 3.0 mm electrode separation, was obtained from material cut from neighboring wafers of the same crystal. These samples also have E_ρ values in proportion to the separation of the contacts.

3. Signal Saturation at E_ρ

Another method used to demonstrate the response time changes with bias was to operate the signal diode at a frequency well above the reciprocal of the dielectric relaxation time constant. The data plotted in Figure 8 include signal versus bias data at low frequencies for comparison.

The 15 Hz curve is a total, fast plus slow, response curve and shows super-linearity seen for devices near E_ρ. At the higher frequencies a saturation of the signal is seen. The small turnup at the higher biases for the 15 kHz curve occurs from the increasing low frequency signal. This arises as the signal has a slow component of amplitude $A_\rho(E)$ with time constant τ_ρ, and a fast component of amplitude $A_f(E)$ with a time constant τ_f. Thus the signal i_s has the form

$$i_s = \frac{A_\rho(E)}{(1 + \omega^2 \tau_\rho^2)^{\frac{1}{2}}} + \frac{A_f(E)}{(1 + \omega^2 \tau_f^2)^{\frac{1}{2}}} \qquad . \qquad (11)$$

At 15 kHz for much of the bias range $\omega \tau_\rho > 1$ and $\omega \tau_f \ll 1$, so that the expression for the signal reduces to

$$i_s = \frac{A_\rho(E)}{\omega \tau_\rho} + A_f(E) \qquad . \qquad (12)$$

With increasing bias, after A_f has saturated, the increasing first term will eventually be detected. By going to a still higher frequency, 150 kHz, the first term is reduced to negligible values even at the highest biases employed.

14
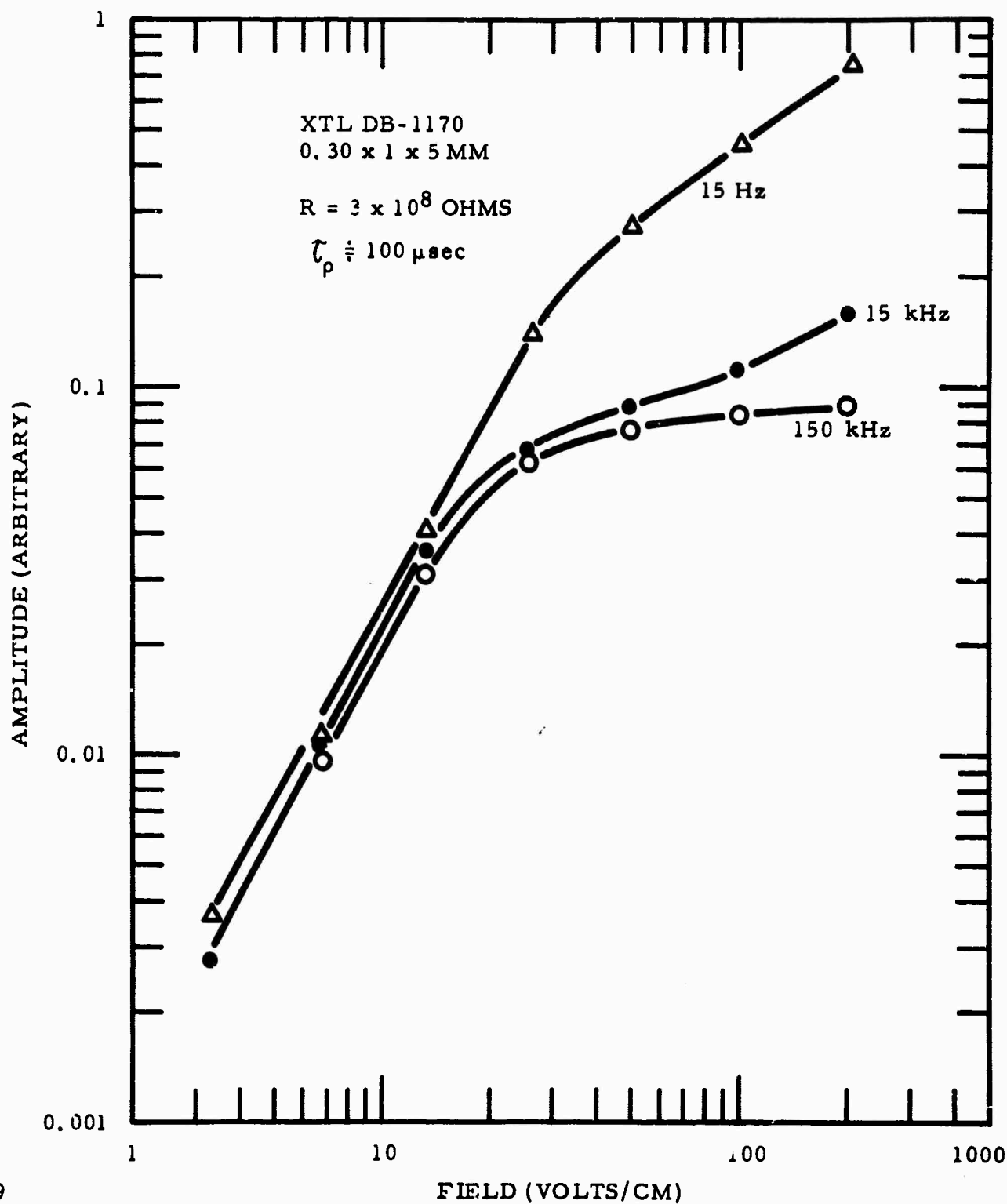
Figure 8   Variation of the Total Signal, 15 Hz, and the Fast Component,
15 kHz and 150 kHz, with Bias. With high frequencies the slow
component of the signal is not seen. Saturation of the signal
corresponds to the onset of the dielectric relaxation effects.

5158-9

15

The E_ρ dependence on electrode separation has also been demonstrated using hi. frequency signal versus bias data, such as that reproduced in Figure 9. As noted above, at 150 kHz the frequency of measurement is well above the reciprocal of τ_ρ. This is so because with a typical resistivity of the order of 100 megohm-cm, the τ_ρ value is approximately 10^{-4} second. The plot of i_s/V removes the bias dependence of the amplitude and reflects the change of the signal from fast to slow. The high frequency component of i_s/V increases somewhat until the E_ρ range is attained; then it decreases. For the thinner sample, the decreasing portion of i_s/V curve occurs at fields about one order of magnitude lower than those for the thicker units.

The rising portion of the i_s/V curve below E_ρ represents the field dependence of the hole lifetime or the mobility-lifetime product. Such field dependencies tended to mask the transition from fast to slow signals, complicating interpretation of responsivity-bias data. These field dependent responsivity effects are more fully discussed in a later section of this report.

4. Photosensitivity for Electric Fields Near E_ρ

Detailed photosensitivity measurements were performed on the various crystal samples to determine their mobility-lifetime product $\mu_p \tau_\ell$ (Table I). This product has been calculated from the expression for the current responsivity i_s, namely

$$i_s = q\mu_p \tau_\ell V\varphi\eta A/L^2 \quad . \tag{13}$$

where φ is the photon flux density, A the detector area, and L the electrode separation; η, the efficiency, includes losses through the dewar window, loss due to reflection from the detector surface, and a factor for incomplete absorption in the crystal. Data used for the efficiency parameter are given at the bottom of Table I. The product $\mu_p \tau$, determined from photosensitivity is compared in Table I to a value calculated from E_ρ. At this value of the electric field the drift length of carriers must be of the order of the electrode separation; thus, $\mu_p \tau_\ell = L/E_\rho$.

5425-1
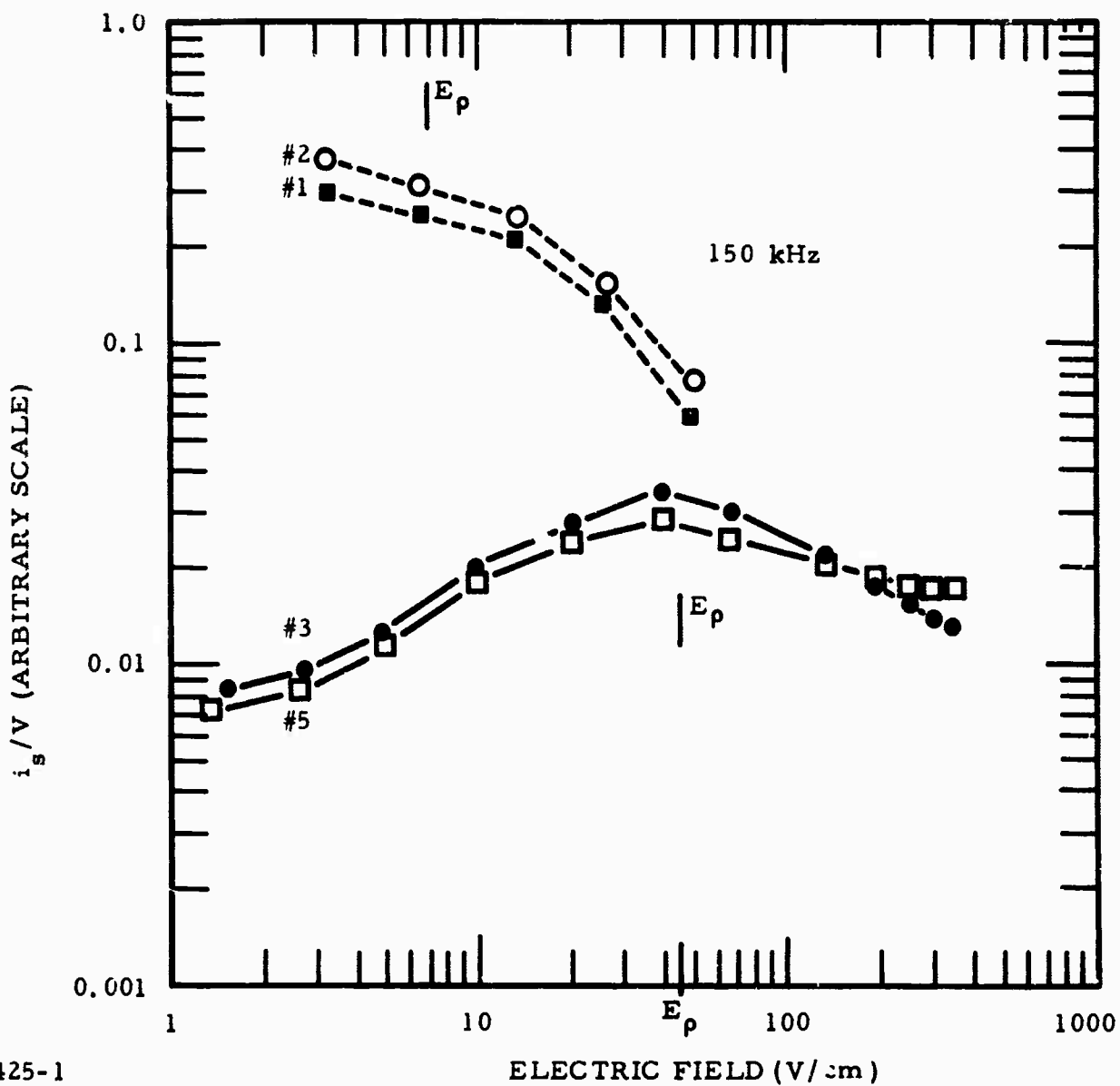
Figure 9 Fast Component Vari·tions with Electric Field for Different Electrode Separations. The ma.·mum in the high frequency responsivity curve corresponds to the onset of the dielectric relaxation effects for the 3.0 mm elements. With the 0.33 mm elements only the fall-off of the responsivity is seen, since it occurs at approximately one order of magnitude smaller electric field.

17

TABLE I

Comparison of Mobility-Lifetime Product Values From Photosensitivity
and Dialectric Relaxation Phenomena

Crystal No.	L (mm)	E_ρ (V/cm)	L/E_ρ (cm^2/V)	$\mu_p \tau_\ell$ (cm^2/V)	$\dfrac{\mu_p \tau_\ell}{L/E_\rho}$
K-70	3.0	10	3×10^{-2}	1.7×10^{-2}	0.6
B-56	3.0	45	7×10^{-3}	3×10^{-3}	0.4
A-48	1.0	15	7×10^{-3}	1.3×10^{-2}	1.8
B-56	1.0	7.5	1.3×10^{-2}	9×10^{-3}	0.7
A-84	1.0	15	7×10^{-3}	6×10^{-3}	0.9
1170-In	1.0	100	1.0×10^{-3}	2.2×10^{-3}	2
1170-AuGa	1.0	800	1.2×10^{-4}	1.2×10^{-4}	1.0
A-48	0.33	45	7.3×10^{-3}	6×10^{-3}	0.8
B-56	0.33	5.0	6.6×10^{-3}	2×10^{-3}	0.3
1170	0.33	15	2.2×10^{-3}	8×10^{-4}	0.4
A-30	0.33	25	1.3×10^{-3}	9×10^{-4}	0.7
Cu-7	0.33	85	3.9×10^{-4}	1.0×10^{-4}	0.3
X-17	0.33	160	2.1×10^{-4}	1.5×10^{-5}	0.08

Average   0.8

Calculated Efficiencies

Window Transmission $\eta_w = 0.45$

Transmission at Germanium Surface $\eta_s = 0.64$

Absorbed in Detector $(1 - 1/e)$ $\eta_a = 0.63$

Net Efficiency $\eta = \eta_w \eta_s \eta_a = 0.18$

18

The two methods of evaluating $\mu_p\tau_\ell$ are compared in the extreme right column of the table. This is the ratio of the $\mu\tau$ product calculated from photosensitivity to the value calculated from E_ρ. While there is scatter in the values, the average value of 0.8 indicated good correlation between the drift distance S at E_ρ and the electrode separation L. The absolute value of the ratio, 0.8, is not as significant as the fact that the same value of this ratio is obtained for materials having $\mu\tau$ values differing by two orders of magnitude and for electrode separation differences of a factor of 10. The value for crystal X-17 is not in good accord with this average, but because of the extremely low value of $\mu_p\tau_\ell$ it is hard to judge the significance of this result.

Note the copper-doped germanium sample in the 0.33 mm group in Table I. The behavior of the copper-doped germanium sample has been identical to that of the mercury-doped germanium sample in terms of appearance of the dielectric relaxation effects.

5. Summary of Dielectric Relaxation Effects

The onset of dielectric relaxation effects occurs at an electric field for which the photogenerated carriers drift a significant portion of the interelectrode spacing before recombination. From the data in Table I we find that the 50% value of the slow-fast rates A_ρ/A_f occurs for a drift distance of 80% of the interelectrode spacing. This figure is subject to revision since the scatter in the data is a factor of 2 on each side of the 0.8 value.

6. Electric Field Dependence of Mobility-Lifetime Product

An extensive study was conducted of the field dependence of direct current resistance and photosensitivity to determine if variations observed could be identified with the transition to the dielectric relaxation regime.

With reduced backgrounds, signal versus bias data were taken at 15 Hz, a frequency sufficiently low to prevent response time limitations. The load resistance was at least two orders of magnitude smaller than the detector resistance so that photocurrents i_s were measured. The data are plotted as the ratio i_s/V so that $\mu_p\tau_\ell$ variations are examined [c.f. Equation (13)].

19

Figure 10(a) is a plot of i_s/V data for 0.33 mm elements along with the reciprocal of the detector resistance, both plotted aga.nst the electric field. The E_ρ values obtained for this detector are marked on the graph. There is a general increase in the sensitivity of the material with bias, but it appears to be a linear function of E with no specific variation associated with E_ρ.

Figure 10(b) is similar to 10(a) but concerns 3 mm elements. A wider range of observations was obtained with the thicker elements because high bias levels could be applied. Note that the linearly increasing sensitivity portion of curves for the 3 mm elements centers about E_ρ.

The striking feature of the curves of Figures 10(a) and 10(b) is the identical nature of the enhanced sensitivity found at higher bias levels for both low frequency signal responsivity and resistance measurements. This has a very significar consequence.

The resistance of an extrinsic germanium photosensitive element is determined by the background flux density φ_B through the relationship.

$$R = \frac{L}{w} \; \frac{1}{q \eta \varphi_B \mu_p \tau_\ell} \tag{14}$$

(w is the width of the element). The product of current responsivity [Equation (13)] times the detector resistance, [Equation (14)], is the open circuit photoconductive signal voltage v_s and is given by

$$v_s = \frac{\varphi_s}{\varphi_B} V \quad . \tag{15}$$

Similarly, the form for the photocurrent and the direct current I is

$$i_s = \frac{\varphi_s}{\varphi_B} I \quad . \tag{16}$$

Clearly, photoconductivity will appear linear when open circuit voltages versus bias voltage or short circuit currents versus detector current are plotted.

20
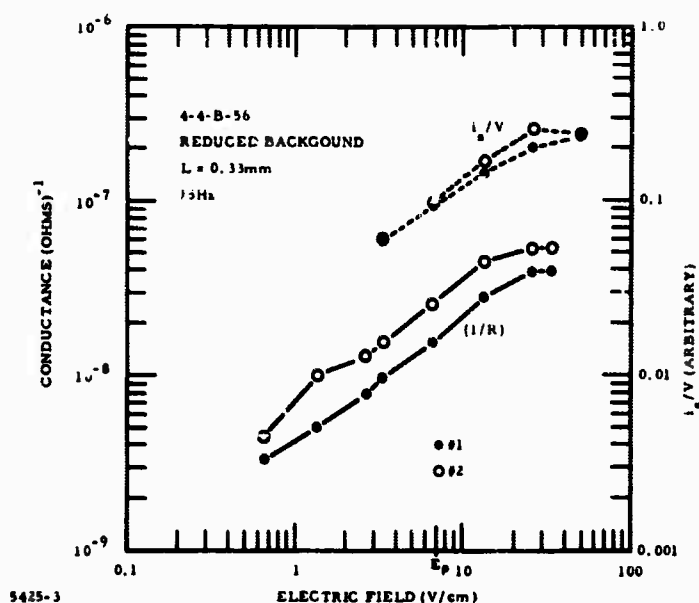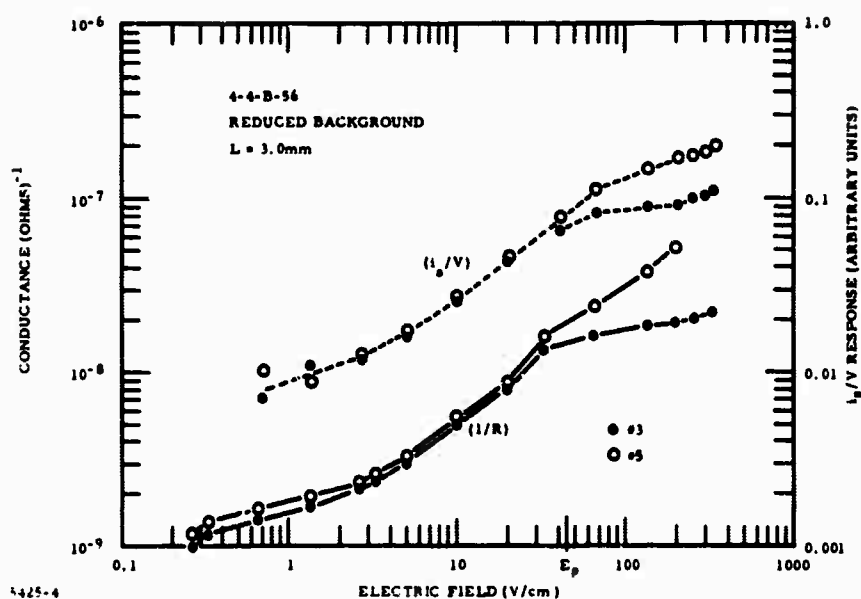
Figure 10   Field Dependence in Reduced Background of the Low Frequency Responsivity and Conductance, (a) 0.33 mm and (b) 3.0 mm Elements. The responsivity, measured at low frequencies to include all the frequency components, increases nearly linearly with the electric field. The direct current conductance has essentially the same field dependence. The wide range of measurements obtained with the 3.0 mm elements, (b), suggests that the strongest field dependence of responsivity occurs for field around E_ρ ($A_\rho/A_f = 1$).

21

With increasing background intensities there appears to be less field-dependent sensitivity, and it is harder to identify the changes with E_ρ values. Figure 11(a) is a plot of data for 0.33 mm elements, and Figure 11(b) shows data for 3.0 mm units. For this set of curves the background was that of 300°K, 180° field-of-view operation. It is easier to identify the sensitivity peaks with a field of 30 to 40 V/cm than with E_ρ.

As strong mobility field dependencies arise above the 30 to 40 V/cm range,[4] interpretation of the sensitivity variations is difficult. However, as mobility falls off with high fields, the enhanced sensitivity is associated with carrier lifetime. While data such as in Figures 10(a) and 10(o) hint at a correlation between the sensitivity increase and the dielectric relaxation effect, this correlation cannot be taken as definitely established. For low sensitivity materials 30 to 40 V/cm fields are reached before E_ρ. Little variation in sensitivity is observed for these materials with increasing electric field.

D. Conclusions

From the data presented it is clear that space charge and dielectric relaxation effects occur as the result of sweepout of holes in mercury- and copper-doped germanium. These effects arise when the drift length of the carriers becomes comparable to the electrode separation, that is, when the photoconductive gain approaches unity. With the higher lifetime materials so that sweepout occurs before mobility becomes field dependent, there are indications of lifetime changes near E_ρ.

It is apparent that only with the low absorption coefficient extrinsic detectors can the dielectric relaxation effects be seen because the resistivity of the extrinsic photoconductor is approximately equal numerically to the resistance of the sample. For intrinsic photoconductors, sample thicknesses of microns are employed, and the resistivity of the material has a value 10^{-4} of the resistance of the sample. Stray capacitance results in much longer response times for intrinsic photoconductors than the dielectric relaxation effects.

22
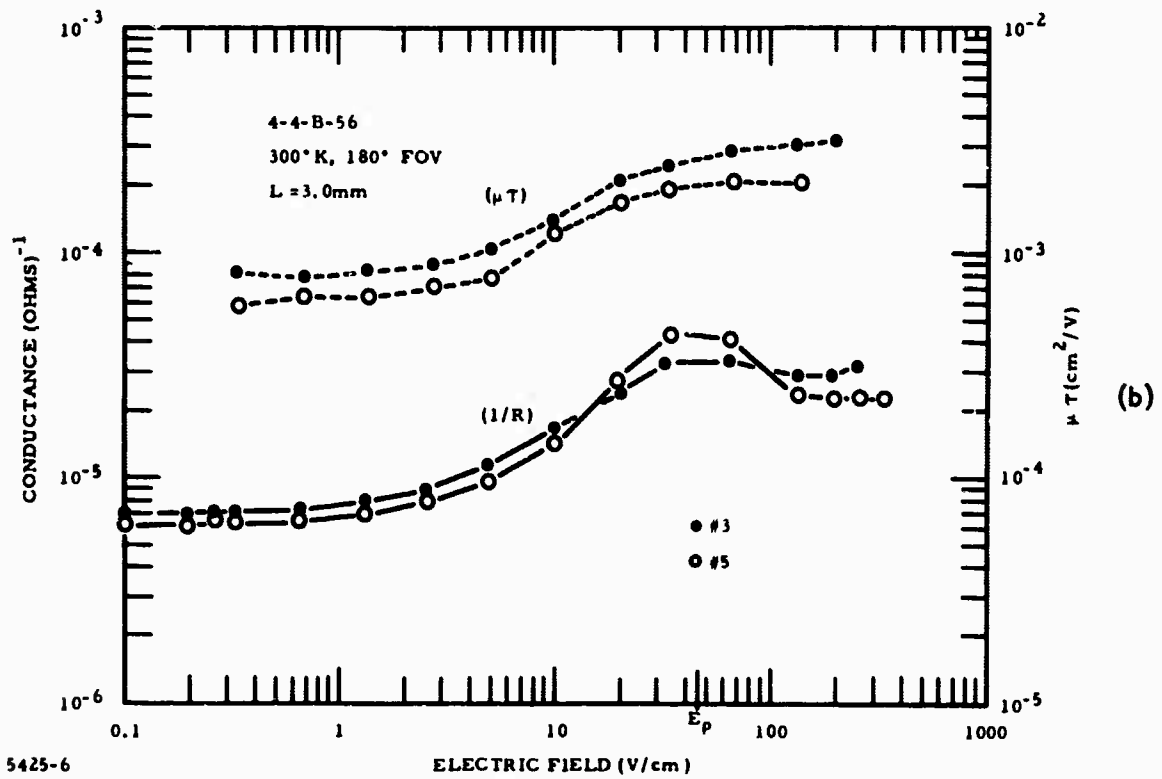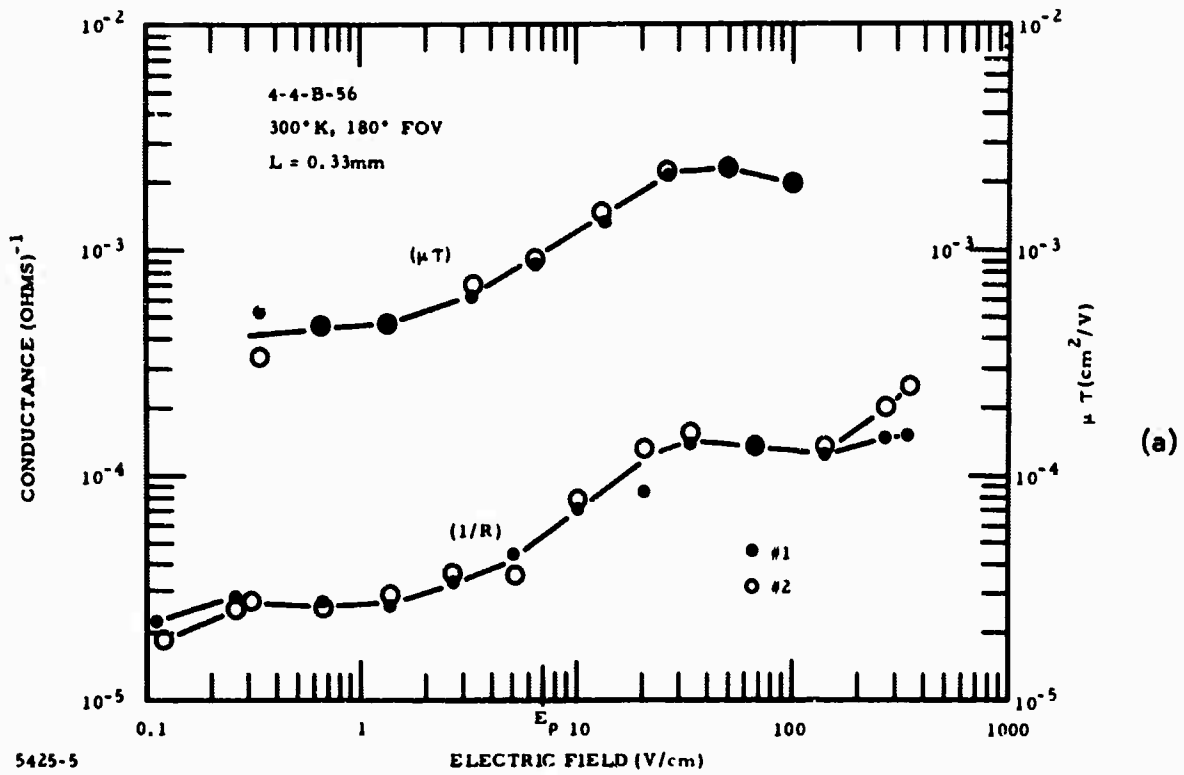
Figure 11 Field Dependence, in a 300°K, 180° Field-of-View Background, of $\mu_p \tau \ell$ and Conductance of (a) 0.33 mm and (b) 3.0 mm elements. There is a field dependence of the parameters plotted, but for this case it appears to be solely a field phenomenon.

23

SECTION II

SPEED AND S: SITIVITY CONSIDERATIONS

A. Extrinsic Photoconductor

1. Introduction

The study of dielectric relaxation effects clearly shows that speed can be limited if Ge:Hg and Ge:Cu detectors are operated in the high bias range. For the operating conditions of drift length greater than electrode separation the dielectric relaxation time constant component predominates   Further, in this mode of operation sensit:vity and speed are interrelated.

2. Detector Speed-Dielectric Relaxation Time Constant

The response of the detector always contains a dielectric relaxation component. This component is usually small or is sufficiently fast to be of no concern. In two situations, high speeds and low backgrounds, it can be the dominant response time. In the latter situation the reduced background increases the dielectric relaxation me to values as long as seconds.

The dielectric relaxation time is given by

$$\tau_\rho = \epsilon \epsilon_o \rho \qquad ,$$

where ρ is the resistivity of the material, ϵ the dielectric constant, and ϵ_o the permitivity of free space. The dielectric relaxation effects are delays so that the total response time τ of a detector is the sum of the carrier lifetime τ_ℓ and τ_ρ. Thus,

$$\tau = \tau_\ell + \tau_\rho \qquad . \tag{17}$$

For extrinsic photoconductors the resistivity of detector materials is determined by the background flux φ_B, namely

$$\rho = \frac{1}{\varphi_B \eta \tau_\ell \mu_p q} \qquad . \tag{18}$$

24

In this expression η is the efficiency with which the radiation is absorbed, t the sample thickness, μ_p the hole mobility and q the electronic charge. Combining Equations (17) and (18) yields

$$\tau = \tau_\ell + \frac{\epsilon\epsilon_o t}{\varphi_B \eta \tau_\ell \mu_p q} \qquad . \qquad (19)$$

This equation is plotted in Figure 12 as a function of φ_B expressed in photons/sec/cm^2 and in watts/cm^2 of 10.6 μ radiation.

Some interesting results are immediately apparent from Figure 12. For 300°K background radiation, if the detector lifetime is less than 2×10^{-8} sec, the response time will be longer than 2×10^{-8} sec. Further, for 10^{-10} sec material there is a response time component of 10^{-6} sec. Figure 12 indicates that if speeds faster than 2×10^{-8} sec are to be realized, the background flux must be increased above the 300°K background value. It is noteworthy that a speed of 10^{-10} sec requires a background flux of 100 watts/cm^2. These considerations apply if the photoconductive gain is greater than unity. Even with material having a lifetime of 3×10^{-9} sec, gain in excess of unity has been realized. Our experiments indicate that if we are prepared to accept low responsivity -- that is, gains significantly less than unity -- the detector will be fast.

3. D^* - Speed of Response Considerations

A consequence of the response time arguments in Section I is that D^* and the fastest speed of response are related because there is an optimum carrier lifetime for each background photon flux. This can be seen by plotting Equation (19) in another way. In Figure 13 the response time is plotted as a function of carrier lifetime for several values of background flux. It is clear that for a fastest response time τ_{min} there is an optimum carrier lifetime τ_{opt}. The minimum response time for a particular background is obtained by equating the two terms of Equation (17), namely

$$\tau_\ell = \tau_\rho \equiv \tau_{opt} \qquad . \qquad (20)$$

25
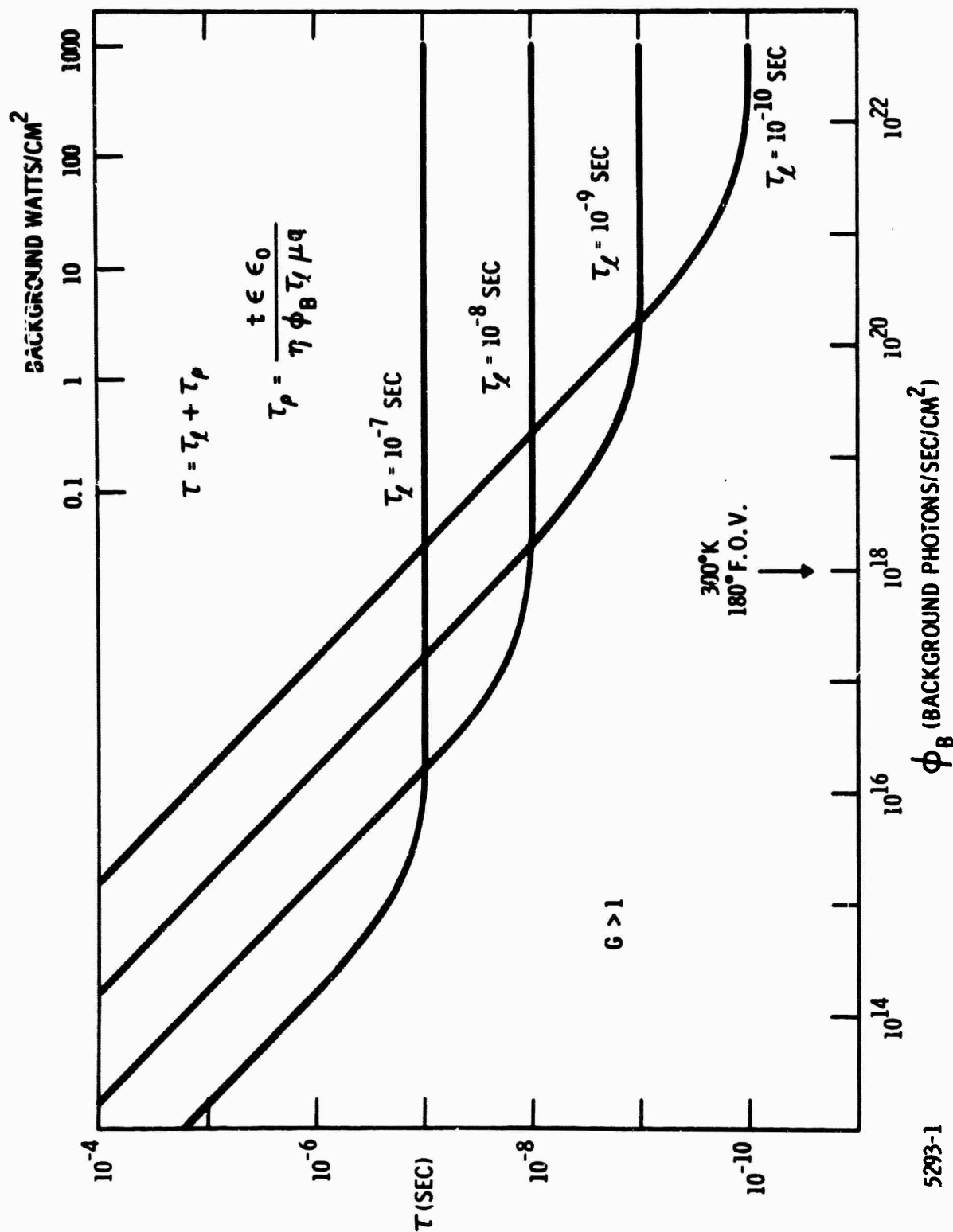
Figure 12 Total Detector Response Time. Because of dielectric relaxation effects the detector response time varies with background photon flux. At low flux densities, when the response time is determined by the background, the shortest lifetime material has the longest response time.

5293-1

26
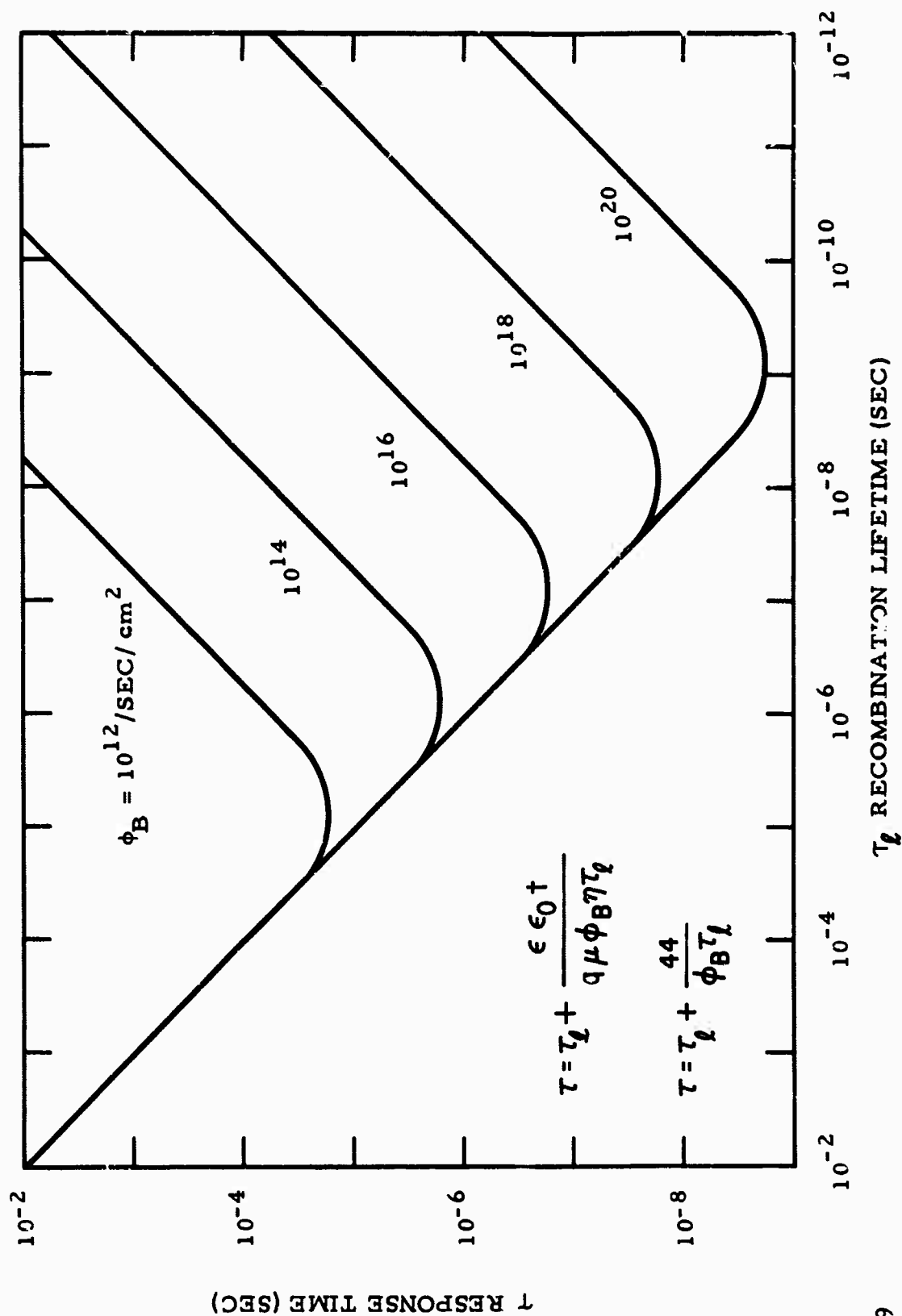
Figure 13 Variation of Response Time with Recombination Lifetime. For a particular background flux the response time depends on the carrier lifetime, being long if τ_ℓ is too short or too long. The fastest response time requires a specific carrier lifetime for each background value.

Thus,

$$\tau_{\ell opt} = \left(\frac{\epsilon\epsilon_o t}{q\mu_p \eta\varphi_B}\right)^{\frac{1}{2}} \quad . \tag{21}$$

Recognizing that $\tau_{min} = \tau_\ell + \tau_\rho = 2\tau_{\ell opt}$ is the minimum response time,

$$\tau_{min} = 2\left(\frac{\epsilon\epsilon_o t}{q\mu_p \eta\varphi_B}\right)^{\frac{1}{2}} \quad . \tag{22}$$

The background-limited infrared performance (BLIP) of a detector is given by the following relationship:

$$D^*_{BLIP} = \frac{\lambda}{hc}^{\frac{1}{2}} \sqrt{\frac{\eta}{\varphi_B}} = D^*_{max} \quad . \tag{23}$$

The D^* bandwidth product is then

$$\frac{D^*_{max}}{\tau_{min}} = \frac{\lambda}{hc} \frac{\eta}{4} \sqrt{\frac{q\mu_p}{\epsilon\epsilon_o t}} \quad . \tag{24}$$

It is apparent that the D^*-bandwidth product is independent of background flux. Further, if high D^* values are to be obtained, speed must be sacrificed. Conversely, if speed is required, D^* must be sacrificed.

Rather than consider D^*/τ_{opt}, we have plotted in Figure 14 the separate parameters D^*_{max} and τ_{min} extending into the 10^{-10} sec range of response times. Note that at 10^{-10} sec D^* has a value of only 3×10^8 cm(Hz)$^{\frac{1}{2}}$/watt. The graph is applicable for gains in excess of unity.

B. Responsivity and Speed: Photoconductors Versus p-i-n Diodes

In Figure 15 we have plotted the gains that can be obtained from photoconductors and p-i-n diodes. In calculating the gain $G = \mu E\tau/L$ a saturation velocity of 3×10^7 cm/sec has been used in place of μE. The curves indicate

28
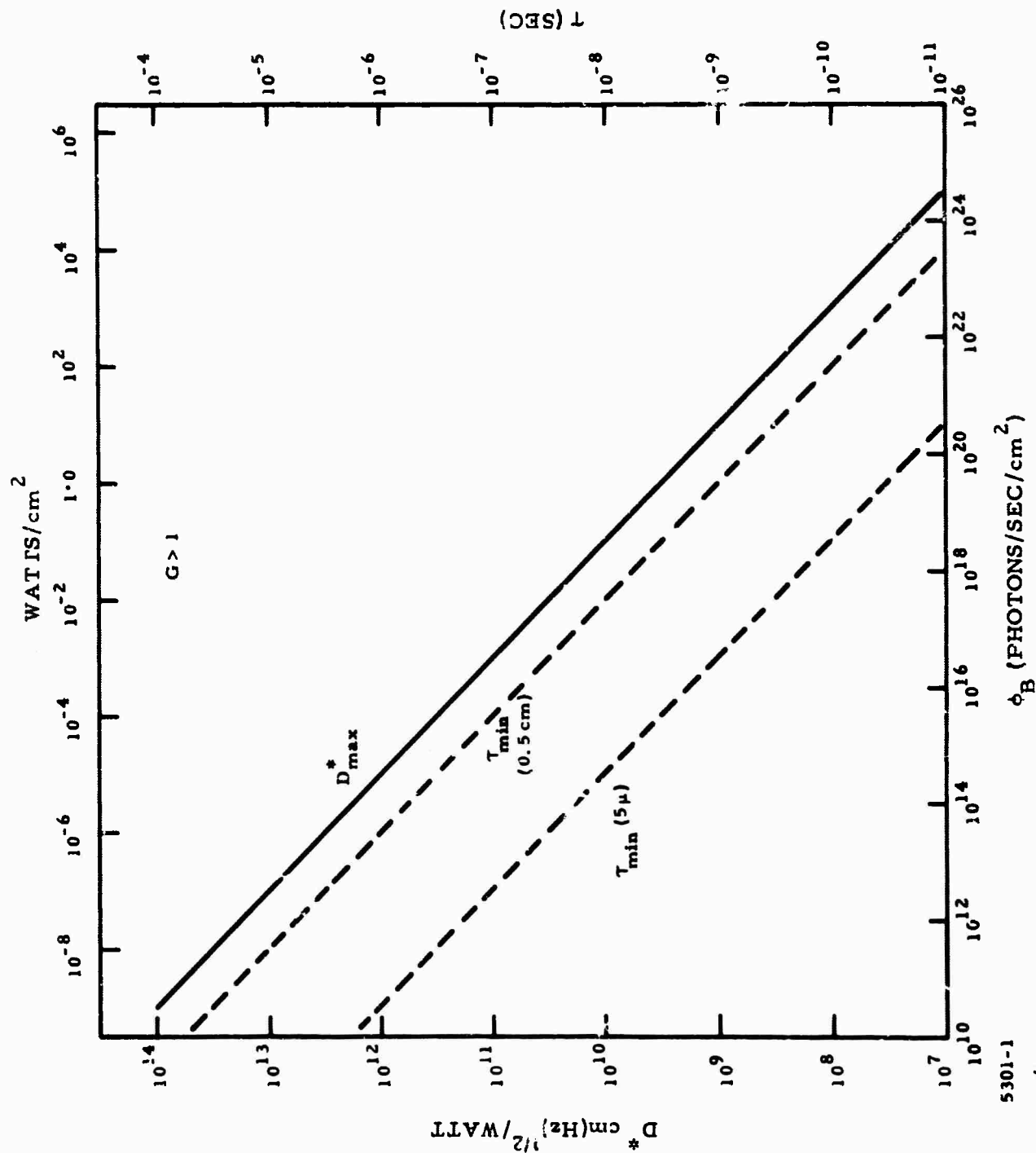
Figure 14 Maximum D* and Minimum Response Time. Under operating conditions with photoconductive gain in excess of unity. dielectric relaxation determines speed of response. Then for background-limited operation both D^* and the minimum response time are determined by the background photon flux density.

29

$$\frac{G}{T} = \frac{\mu E}{L} = \frac{1}{T_L} \doteq \frac{3 \times 10^7}{L}$$

$$G \doteq \frac{\mu E T}{L}$$

$\mu E = 3 \times 10^7$ CM/SEC

$\mu = 2 \times 10^5$ CM^2/V-SEC

$E = 150$ V/CM

APPLICABILITY

(1) DIRECT DET
(2) HETERODYNE

L=100μ
PHOTOCONDUCTOR

p-i-n DIODE

L=1μ

L=10μ

L= 1 MM
PHOTOCONDUCTOR

10^4

10^3

10^2

10^1

$1\cdot 0$

10^{-1}

10^{-2}

10^{-3}

G

10^{-12} 10^{-10} 10^{-8} 10^{-6}

T_ℓ (SEC)

5301-2
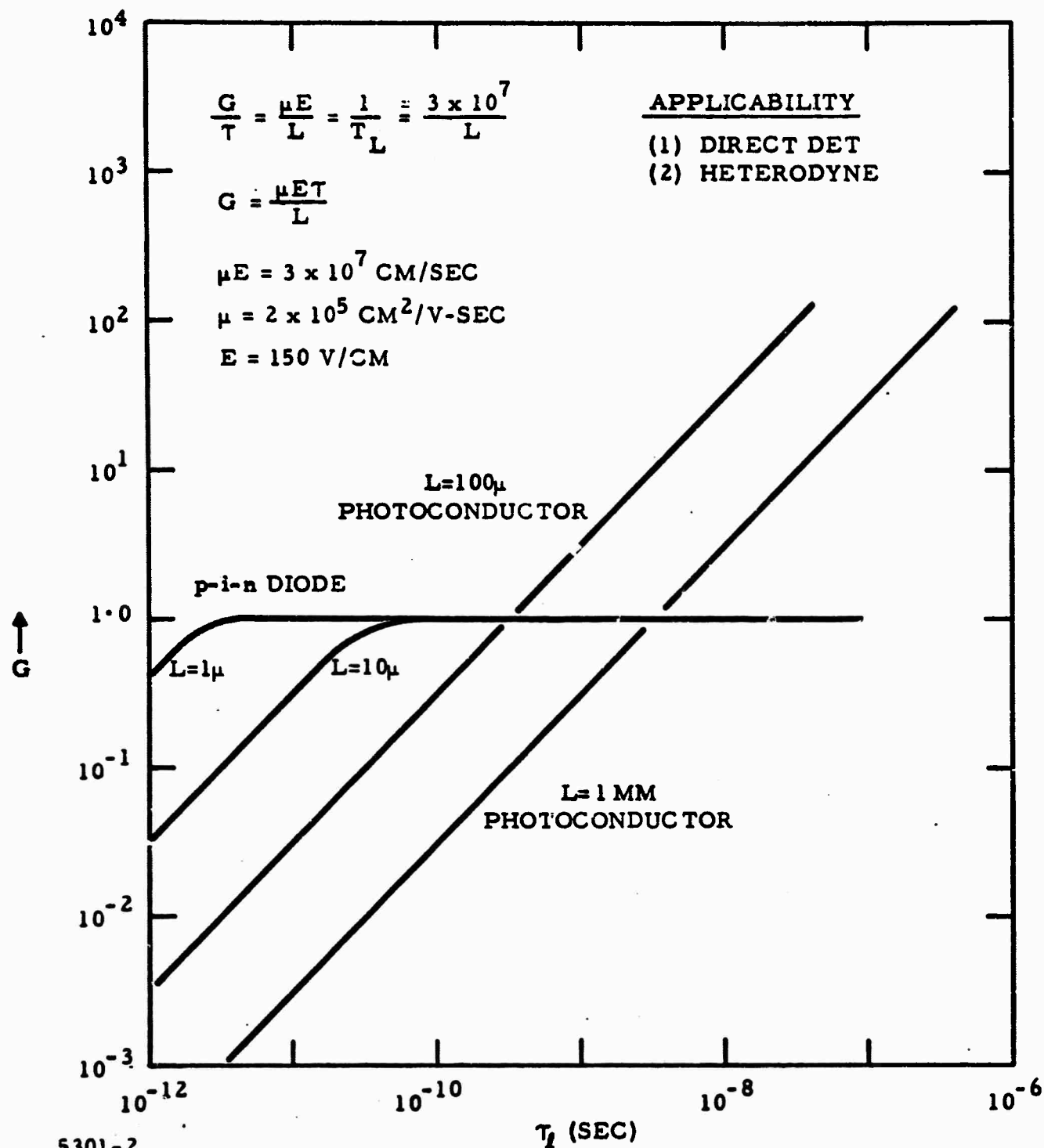
Figure 15   Maximum Gain of Photoconductors and Diodes. When carrier lifetimes become small (10^{-9} sec or less), photoconductive gains reduce significantly below unity, while diodes retain unity gain for carrier lifetimes of 10^{-10} seconds and shorter.

30

that photoconductive gains are likely to be less than unity for material having carrier lifetimes below 10^{-9} sec. By contrast, the speed range of diode with depletion layers of 1 to 10 microns can be expected to extend beyond 10^{-} sec. For high speed, collection by diffusion cannot be allowed; thus, absorption must occur in the depletion region of a p-i-n diode.

C. Conclusions

It is clear from the above arguments that for speeds faster than 10^{-9} second, extrinsic photoconductors are inferior to photodiodes. Since photodiodes in the 0.1 eV range have not yet been optimized, it may well be that extrinsic photoconductors will be employed in this speed range, even with their inefficiencies.

It should also be noted that for the heterodyne detection mode of operation[5-7] local oscillator power may be used not only to achieve heterodyne detection but also to determine background levels and thus the speed of the detector.

SECTION III

CONTACT STUDY

A. Gettering

1.   Introduction

In the early work on dielectric relaxation phenomena[3] nonuniformities
were considered as a possible cause of the effect; therefore, a contact study
was undertaken to establish what role, if any, they play in the phenomena.
It is clear from the analysis presented earlier that sweepout effects rather
than contacts determine the response characteristic. However, the contact
study revealed several interesting features which will be reported in this
section.

2.   Contacts Studied

Three types of contacts were utilized in studying Ge:Hg and Ge:Cu: (1) gallium
diffused layers, (2) gold-gallium alloy layers, and (3) indium solder. All
three types yielded the same dielectric relaxation effects. In the case of gallium
diffused layers on Ge:Hg the contact was not suitable for photoconductivity
studies. In contrast, very good photoconductor performance was obtained with
this contact to Ge:Cu.

The gallium diffusions were performed either in a closed tube using a Ge-Ga
alloy as source, or in an open tube using a GaO_2 source. Diffusion times and
temperatures were varied to produce layers from a fraction of a micron to 5
microns thick. The variations did not appear to significantly influence the
results obtained.

3.   Gettering

The first of the results showed that copper appeared to be gettered from
Ge:Hg wafers by the gallium diffused layer. Such an effect can be anticipated
because of the enhanced Cu solubility in the heavily doped gallium layer.[8]

In preparing Ge:Hg crystals the presence of unwanted impurities is detected by studying resistance (or Hall coefficient)-temperature characteristics. In Figure 16 the resistance of a detector element is plotted versus reciprocal temperature. The "original" curve is non-gallium diffused material which has a slope indicating an activation energy of 0.039 eV. This is less than half the value expected from mercury impurities, which have an ionization energy of 0.088 eV. The deviation arises because of the presence of residual p-type impurities whose concentration is such that the Fermi level is located below the Hg level.

After a gallium diffusion and a short anneal, the material had the resistance-temperature characteristic of the second curve of Figure 16 with an activation energy of 0.075 eV. This is much higher than 0.039 eV, and such material will operate up to at least 40°K, whereas the original material loses its resistance values above 25°K.

The gallium contact studies were difficult because good detectors could not be fabricated utilizing this technique. Current oscillation and nonlinear effects were generally observed at some voltages. This was not the case for Ge:Cu, particularly if excess copper was present during the gallium diffusion. The anomalies observed with the Ge:Hg gallium contacts are believed to be associated with the fact that copper can be a p-type or an n-type impurity. Such a situation can give rise to anomalous structures in the vicinity of a diffusion profile.[9,10]

To ensure that the effects were not surface contact phenomena but were related to an impurity distribution, several ultrasonic bonds were made to the gallium layer on one detector, and the resistance was checked across the gallium layer. The resistance across the surface layer was from 8 to 10 ohms, while each bond contact gave identical anomalous results across the sample.

33
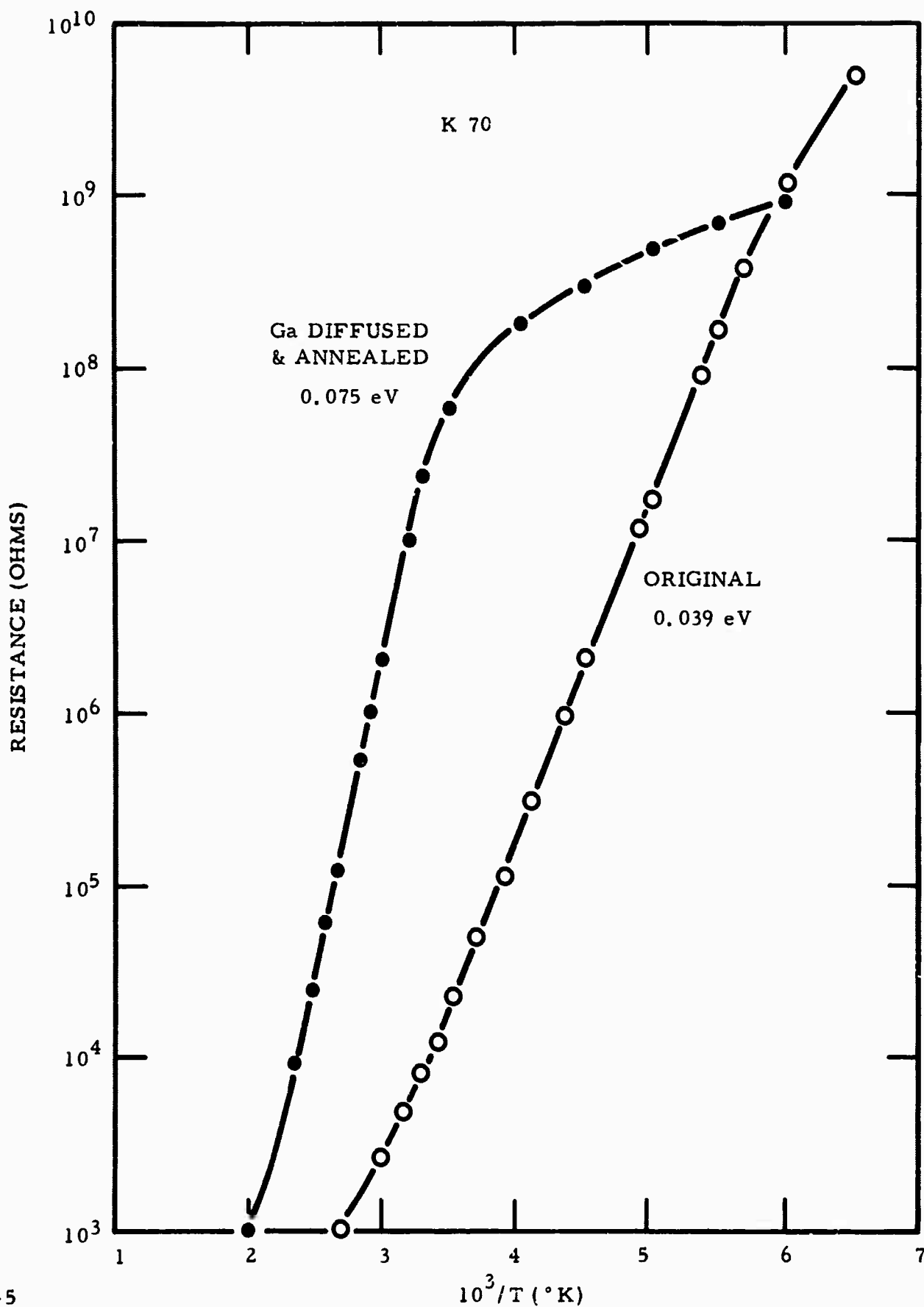
5158-5

Figure 16 Impurity Gettering with a Gallium Diffused Layer. By diffusing gallium
into the surface of Ge:Hg, then annealing, impurities are removed.
An improved resistance-temperature characteristic results. (0.039 eV
activation energy increased to 0.075 eV.)

34

4. Cu-64 Distribution

Radioactive Cu-64 was used to measure the distribution of copper in the surface layer of Ge:Hg wafers containing a gallium diffused layer. The gallium layer was deep to facilitate sectioning. Its depth, 5 microns, was determined by four-point probe measurements taken simultaneously with the Cu-64 determination. The radioactive copper was plated onto one surface of the wafer, which had been lapped to remove the gallium layer. The copper diffusion temperatures and times are given in Figure 17.

To reduce sample edge effects, wafers were 1/4 mm thick and 1.5 cm square. Prior to analysis, the edges were hand-lapped to further minimize edge effects. Standard analysis techniques were then employed to determine the Cu-64 distribution in the surface layer. Two distributions which had the maximum structure are reproduced in Figure 17. Also included in this figure are the four-point probe resistivity measurements for the surface layer of sample A-5.

The error bars on the Cu-64 concentration curves are the errors arising from counting statistics. While they are significant for the smallest concentrations, they are much less than the magnitude of the fluctuations in Cu-64 concentration. The lines with arrows on the resistivity data represent the extreme values of the measurements taken. Only after the first 5 microns had been removed did significant fluctuations in the readings occur, and these were in the range where the Cu-64 fluctuations were found.

Three features of the Cu-64 distribution should be noted: (1) There is a very high surface concentration which is removed by the first etch lap. (2) A very significant maximum-minimum structure is found in the Cu-64 distribution between 3 and 10 microns. (3) The Cu-64 structure extends well beyond the diffused region, to at least 14 microns, with concentrations still well above the average value remaining in the crystal after the last lap shown.

These data indicate that not only is the copper gettered to the surface layer but also that it assumes a very distinct distribution in and beyond the diffused region.
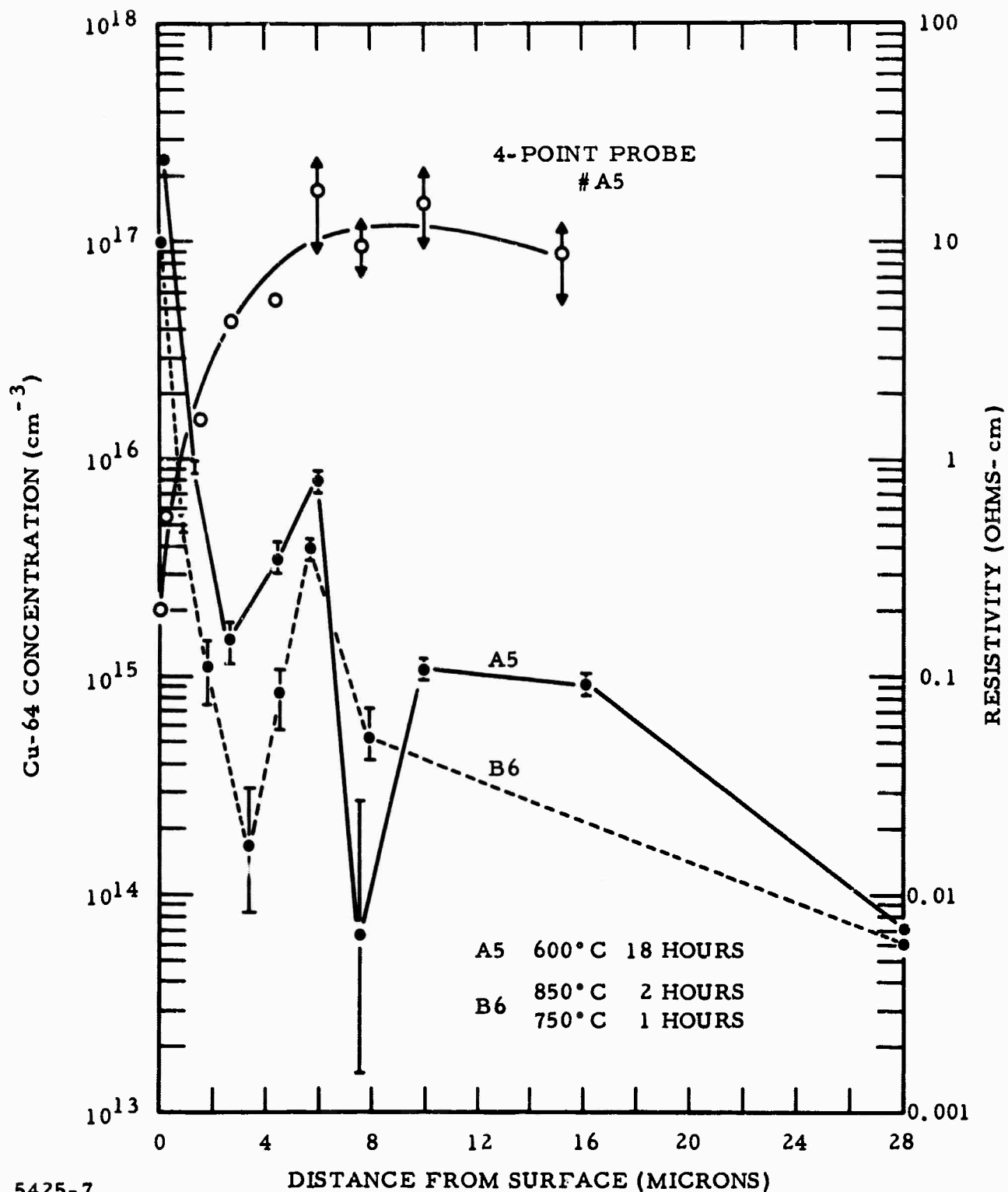
Figure 17 Cu-64 Distribution and Four-point Probe Readings through a Gallium Diffused Layer. With radiochemical techniques and Cu-64, a very significant variation has been found in the copper distribution in and beyond a gallium diffused layer. The four-point probe readings have significant scatter only after 5 microns, the depth of the gallium diffusion.

36

5. Autoradiograms

The distribution of Cu-64 across the surface layer was checked by taking autoradiograms. One such autoradiogram is repioduced in Figure 18. The degree of blackening of the film is a measure of the Cu-64 concentration in the surface layer in contact with the film. The areas that have the sharpest image were in closest contact with the surface of the wafer.

Several large blemishes which are associated with defects appear on the surface, but the rest of the autoradiogram is composed of small blackened regions surrounded by clear areas. While the Cu-64 is distributed fairly uniformly over the surface of the wafer, the autoradiogram indicates that it is localized. Since the gettering action of the gallium layer has been established, it is assumed that the gallium must be localized on the surface as well. However, a very significant drop in Cu-64 concentration occurs just below the surface of the wafer. Thus, the localization may have no counterpart deeper in the material.

B. Photovoltaic Study of Contacts

An idealized p^+ contact is shown in Figure 19(a). The heavily doped region grades to the interior of the crystal and provides a degenerate surface layer to which electrical contact is readily made. If photons of energy greater than the band gap of germanium are incident in this region of the crystal, a photovoltaic response will be obtained because the electrons and holes will be separated by the built-in field of the p^+ - p region. The sign of the photovoltage is indicated on the diagram.

Such a photovoltaic response has been obtained with Ge:Cu having a gallium diffused layer. With the radiation incident on the diffused layer the spectral response was that given in Figure 19(b), with a positive polarity photovoltage. The intrinsic cutoff extends to 1.4 microns, with a significant response beyond this wavelength. The long wavelength response was observed in all cases, but is not yet understood.
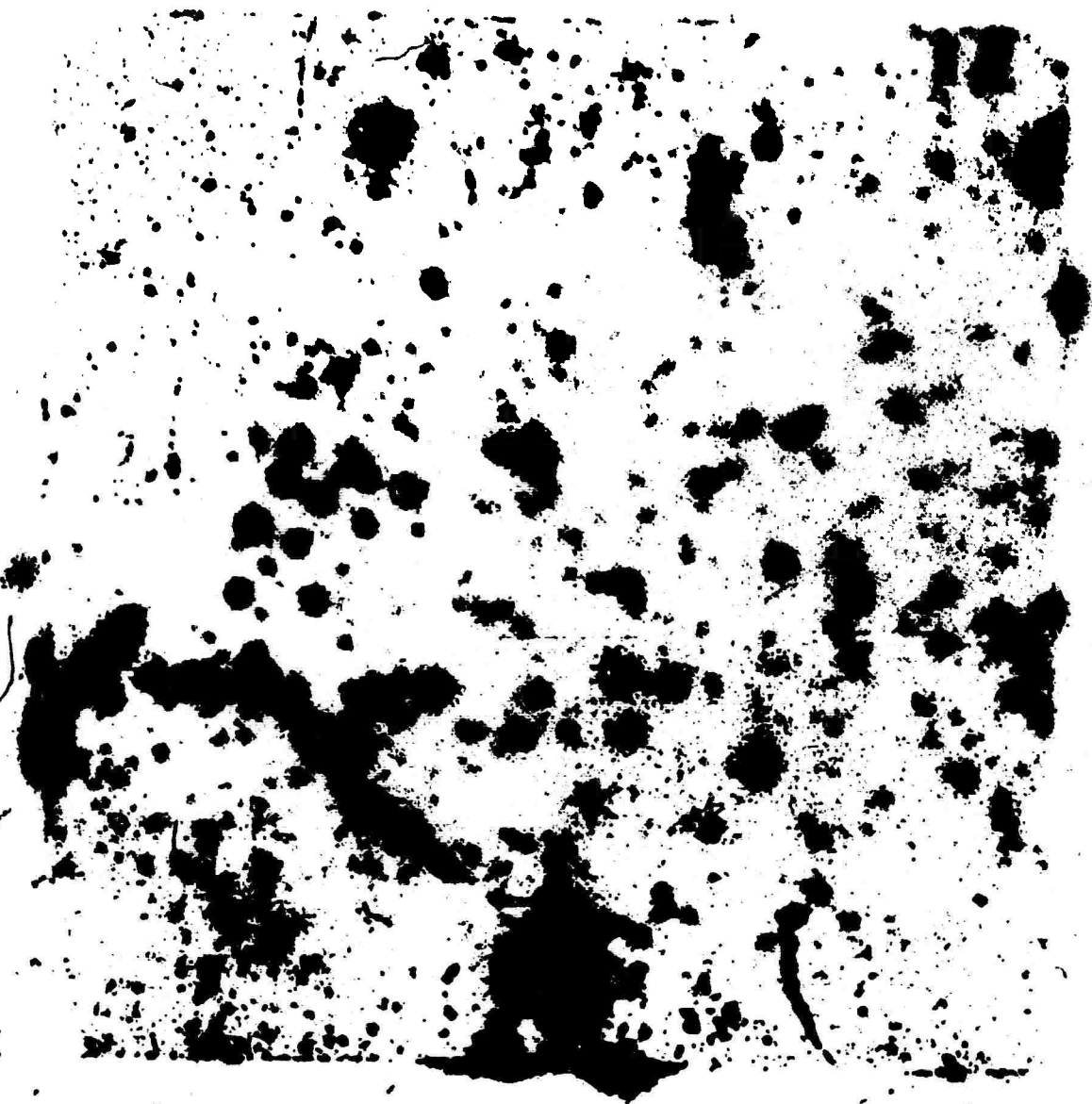
Figure 18 Autoradiogram of Cu-64 on the Surface of a Gallium Diffused Layer.
In addition to the large surface defect regions, the autoradiogram
has recorded the Cu-64 as localized -- the speckled nature of the
autoradiogram. The gallium is assumed to have this nonuniform
nature, but the effect may be only on the surface of the wafer.
The wafer is 1.5 cm on a side.
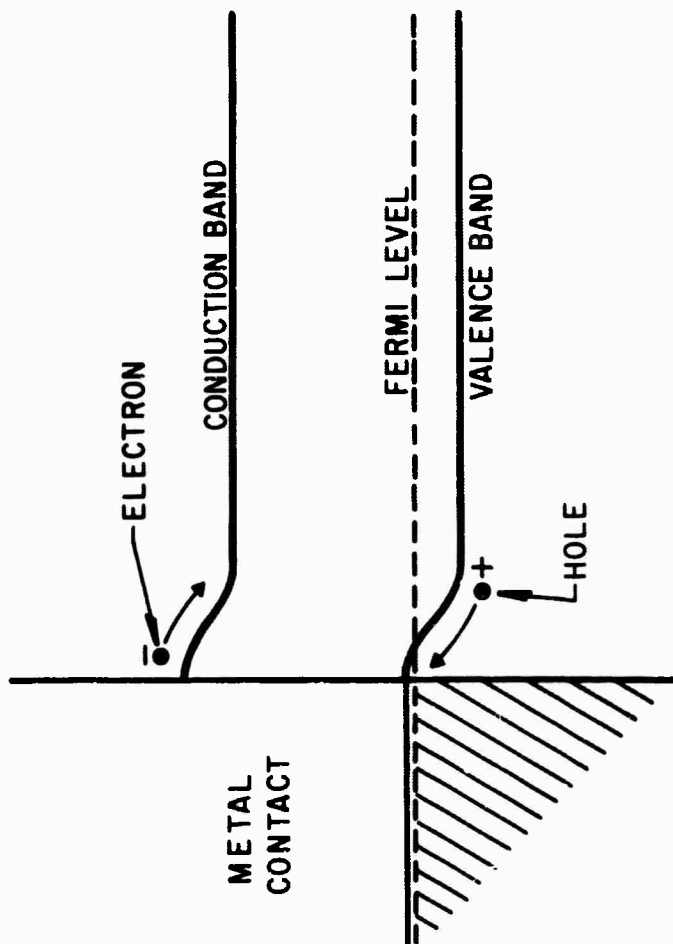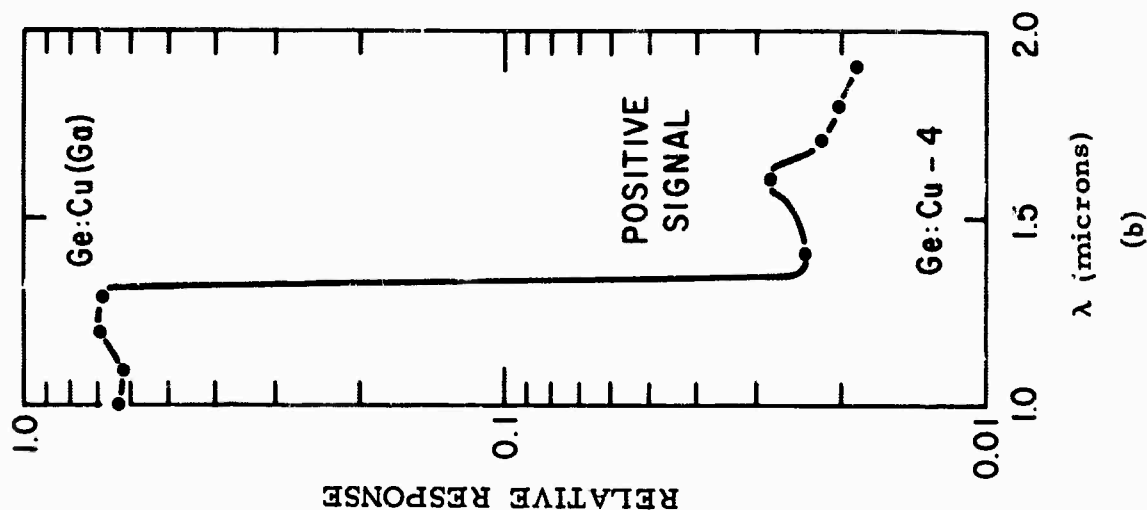
Figure 19 Idealized p^+ - p Contact and the Photovoltaic Response of a Ge:Cu (Ga) Layer. From the p^+ - p structure a positive photovoltaic signal is expected (a). This is observed for a gallium diffused layer on copper-doped germanium (b) (helium temperature).

39

Quite a different result was obtained with Au-Ga alloy contacts to Ge:Hg. The spectral response reproduced in Figure 20(a) is similar to that of Figure 19(b), but the sign is negative, in contrast to the expectation for a $p - p^+$ structure. This result was obtained without exception for three different crystal materials from which at least two samples were tested.

A reverse polarity signal indicates that the potential distribution at the contact is of the form given in Figure 20(b). For such a distribution to exist, the surface must be n-type, or at least less p-type than the bulk. Such a contact would be expected to block the flow of holes into the crystal, but no blocking effects were detected in the I-V characteristics.

These are two possible explanations for this contradiction: (1) The potential dip at the surface may be very shallow, since the photovoltaic measurements were performed at 8 to 10°K. The anomalous region would then have only slightly higher resistance and would not produce major I-V variations (2) Part of the contact area carries the current, while most of the area is blocking.

C. Conclusions

The photovoltaic studies, coupled with the Cu-64 results, indicate that significant structure may be present in the contact area. The anomalies are probably associated with copper distribution in the Ge:Hg samples. Unfortunately, the contact which involves minimum heating (the indium solder contact) is opaque and therefore cannot be probed with radiation. In spite of the anomalies discovered, the dielectric relaxation effects are dependent on sweepout phenomena and are not sensitive to contact structure.

40

P-TYPE PHOTOCONDUCTOR

ELECTRON

CONDUCTION BAND

FERMI LEVEL

VALENCE BAND

HOLE

METAL CONTACT

(b)

Ge:Hg(Au-Ga)

NEGATIVE SIGNAL

DB 1170

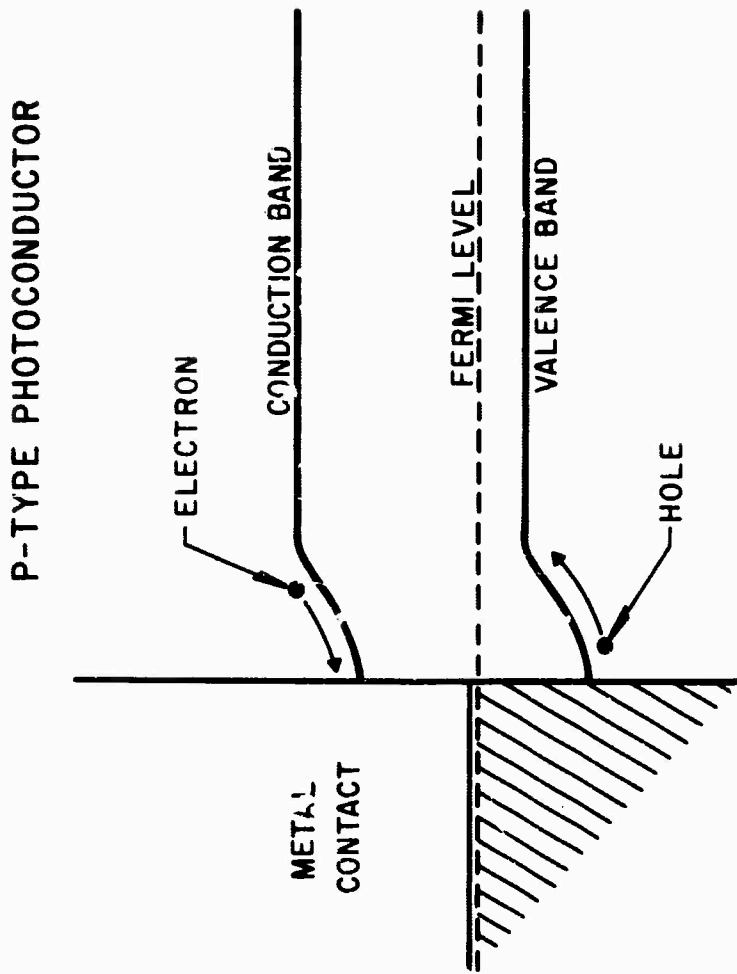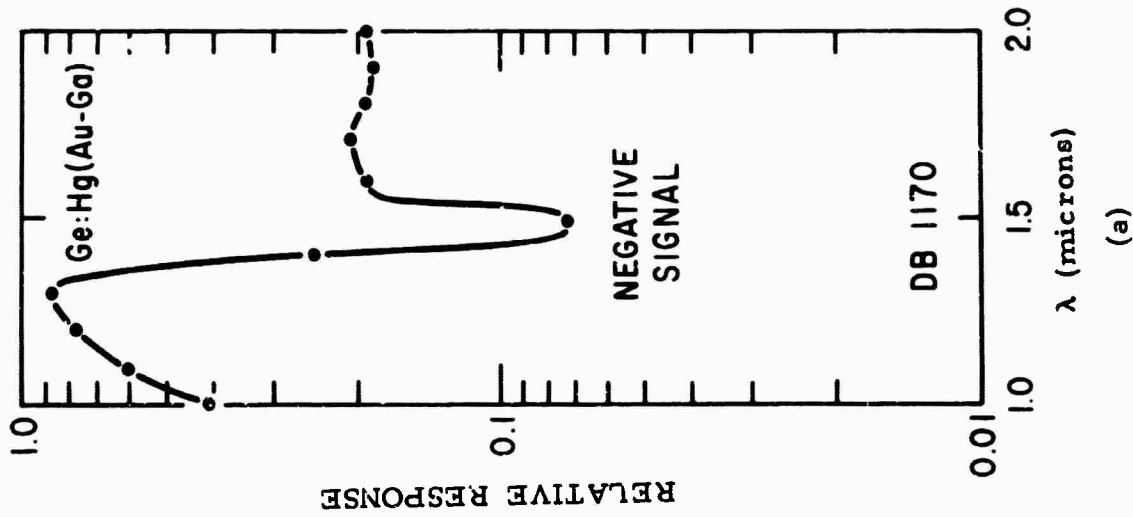λ (microns)

RELATIVE RESPONSE

(a)

Figure 20 Spectral Response with a Gold-Gallium Alloy Contact and the Potential Structure of the Surface Layer. With a gold-gallium alloy layer a negative photovoltaic signal is observed which is of opposite polarity to that expected from a p^+ - p contact (a). To have such a signal polarity the potential near the surface must be of the form shown in (b).

41

SECTION IV

HETERODYNE DETECTION CONSIDERATIONS

A.   Introduction

The heterodyne detection mode of operation is used with coherent radiation sources.[5-7] To achieve high speeds, local oscillator power must be adequate to ensure that dielectric relaxation time constants are short. In addition, special alignment requirements must be met for heterodyne detection, not only angular alignment of the beams but also alignment of the beam on the detector.

B.   Directional Property of Coherent Radiation

One feature of coherent radiation is its parallelism, or its nondivergent character. By contrast, incoherent radiation from the 300°K background is random in direction. The consequence for detector operation can be considerable. Since the local oscillator signal originates outside the detector assembly, it has to be directed onto the detector.

The series of illustrations in Figure 21 details the results of misalignment of the local oscillator signal. Radiation covering only part b of the detector [Figure 21(a)] will give rise to a resistivity profile [Figure 21(b)]. Even when coherent detection is utilized, the 300°K background radiation will still be present. This sets the value ρ_a, while the smaller value ρ_b is determined by the combination of both radiation fluxes. Since sections a and b are in series, the equivalent circuit can be described as shown in Figure 21(c). The signal will be registered as a change of R_b or ΔR_b, while R_a is unaffected even if the signal falls on section a because no coherent radiation reference signal 's present.

For a bias voltage V impressed across the load resistor R_L, the signal voltage ΔV_L appearing across the load is given by the expression

$$\Delta V_L = \frac{R_L \, \Delta R_b \, I}{R_L + R_a + R_b}$$

42

COHERENT
RADIATOR

CONTACT AREA

(a) GEOMETRY

NONILLUMINATED
AREA

ILLUMINATED AREA

(b) RESISTIVITY
PROFILE

R_L

R_a

R_b

V

ΔV_L

(c) EQUIVALENT
CIRCUIT
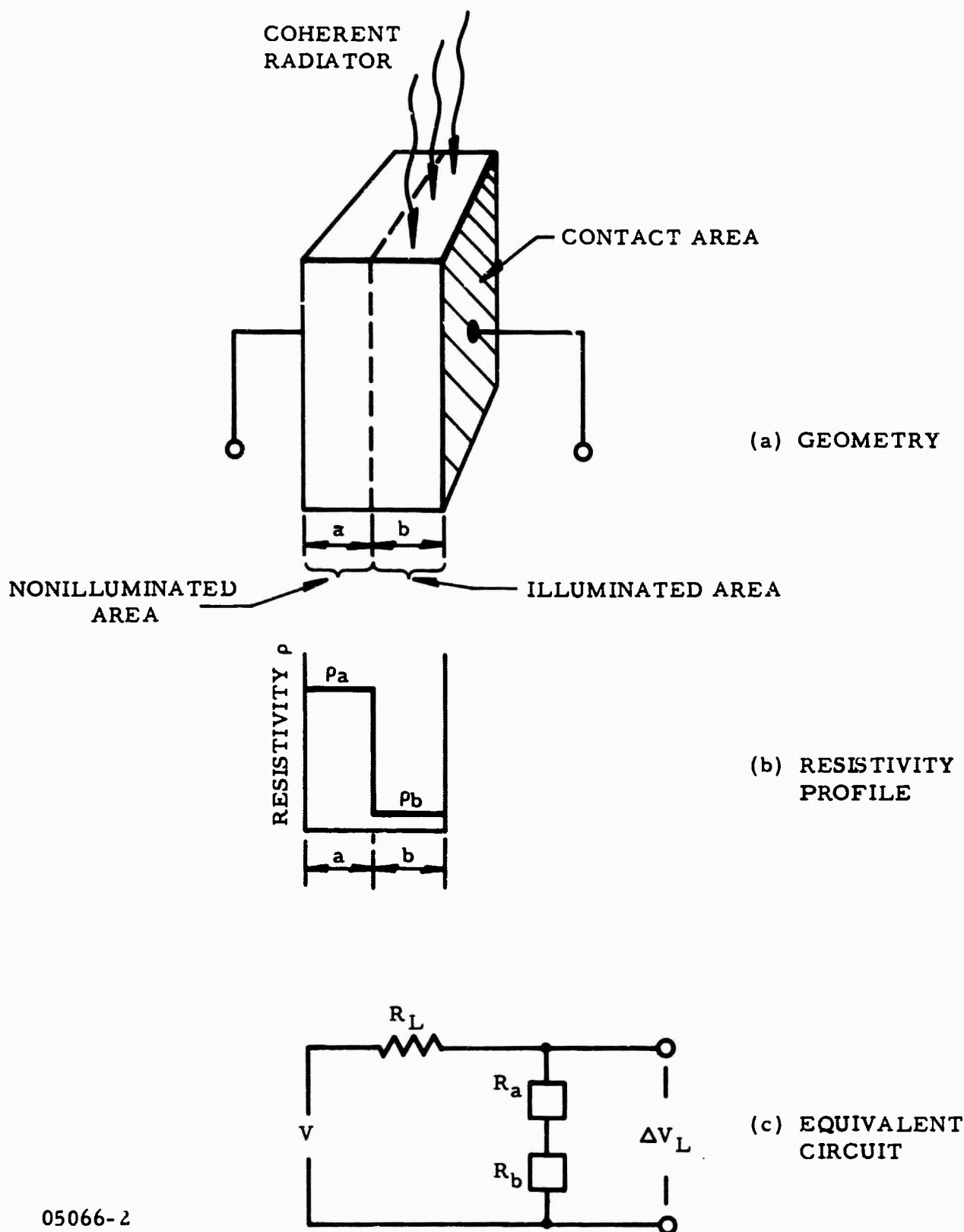
05066-2

Figure 21 Conventional Detector Geometry with Coherent Radiation Incident "Normal"
to the Electric Field. For the local oscillator radiation falling on a
part of the detector (a), a blocking resistance develops (b) and (c),
which reduces the responsivity of the detector.

43

The direct current value is I. For high speeds of operation, R_L is smaller than R_a or R_b to reduce RC effects; thus, usually

$$\Delta V_L \approx \frac{R_L}{R_b} \; \Delta R_b I \; \frac{R_b}{R_a + R_b} \quad .$$

The last factor, $R_b/R_a + R_b$, is a signal reduction caused by the blocking effect of R_a, which will be at least an order of magnitude greater than R_b. For variable background conditions R_b/R_a could have values resulting in serious signal loss variations.

While good system design might reduce the probability of such misalignment, an alternative configuration, shown in Figure 22, eliminates these effects.

C.   Transparent Contacts

In the situation depicted in Figure 22, transparent contacts have been applied to the surface through which the radiation passes. Once again, we consider a local oscillator signal falling only on part _b_ of the detector; thus, the resistivity profile across the detector element will be the same as in Figure 21(b). However, for the contact configuration of 22(a) the appropriate equivalent circuit is that of 22(c) in which the illuminated and nonilluminated areas are parallel resistances.

For this case the signal voltage developed across the load resistor is

$$\Delta V_L = \frac{R_L I \Delta R_b}{\left(R_L + \dfrac{R_a R_b}{R_a + R_b} \right)} \left(\frac{R_a}{R_a + R_b} \right)^2 \quad .$$

For the condition discussed in the previous case, i.e., $R_L < R_b$, R_a, the above expression reduces to

$$\Delta V_L = R_L I \Delta R_b \cdot \frac{R_a}{R_a + R_b} \quad .$$

44

COHERENT
RADIATION

CONTACT AREA

CONTACTS   (a) GEOMETRY

a   b

NC.ILLUMINATED
AREA   ILLUMINATED AREA

ρ_a

RESISTIVITY ρ

ρ_b

(b) RESISTIVITY
    PROFILE

a   b

R_L

V R_a R_b ΔV_L (c) EQUIVALENT
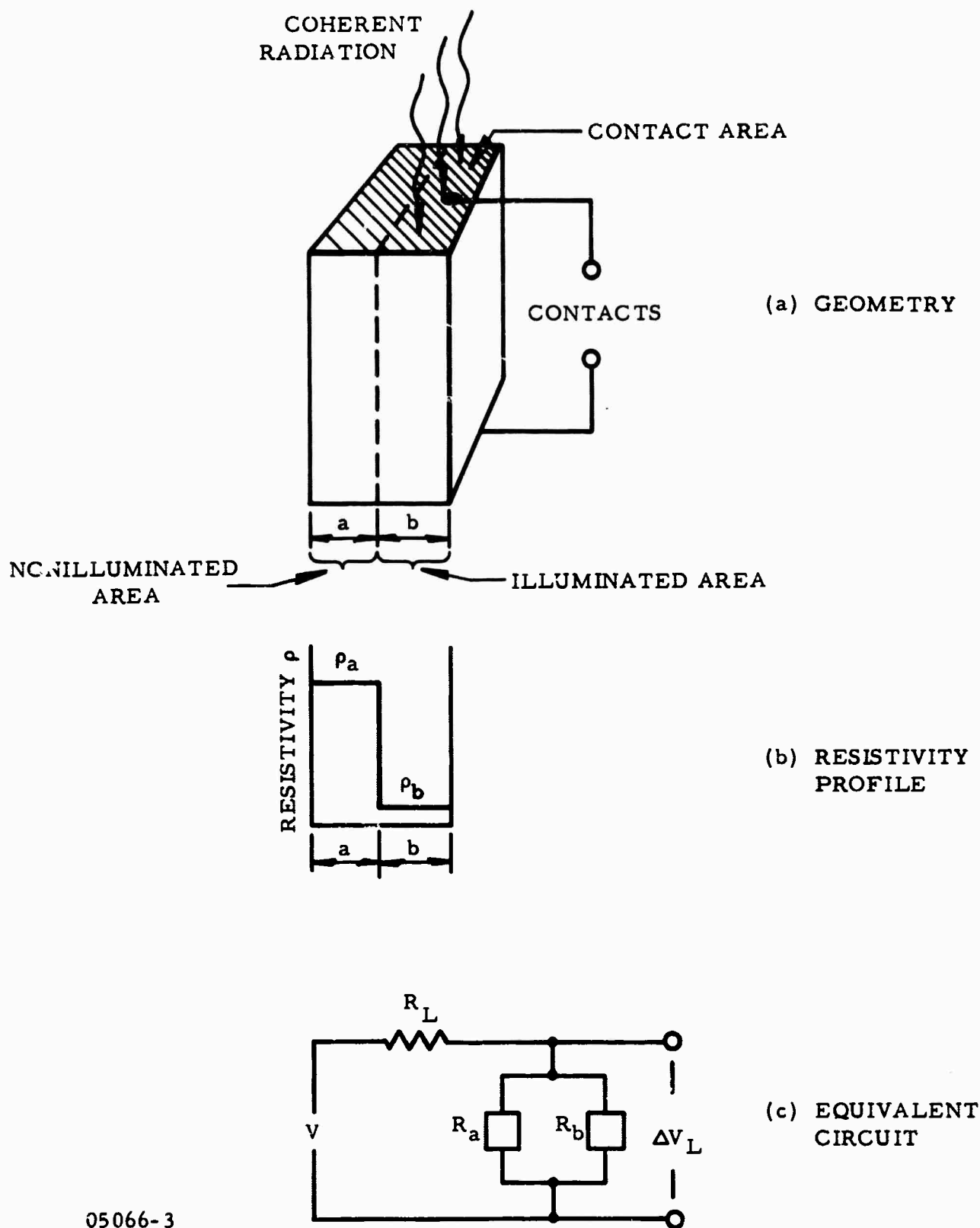   CIRCUIT

05066-3

Figure 22 Collinear Detector Geometry with Coherent Radiation Incident
Collinear with the Electric Field. For the local oscillator
radiation falling on a part of the detector (a), no blocking
resistance occurs (b) and (c).

45

We see that for R_a 10 times R_b only a slight signal loss occurs, and for extreme situations $R_a \gg R_b$ the loss is negligible.

D.   Collinear Mode of Operation

In the mode of operation described above the radiation is incident "collinear" with the device electric field, and in this collinear mode of operation blocking or saturation effects are absent. [In the conventional mode of operation, e.g., Figure 21(a), the radiation is "normal" to the electric field.]

E.   Special Design Considerations Related to the Collinear Mode

Consider a detector material having a carrier lifetime τ_ℓ of 10^{-9} sec and a hole mobility μ_p of 10^5 cm^2/V-sec. Then for an applied bias V of 10 volts across an element thickness L of 1 mm the gain $G = \tau_\ell \mu_p V/L^2$ has a value of 0.1. To achieve high gain or responsivity we require highest voltages of operation and thinnest electrode spacings.

There are two conflicting collinear thickness requirements: (1) small values yield high gain, and (2) large values are needed for high absorption. The value of mercury concentrations in Ge:Hg are generally such that element thicknesses must be at least 1 mm or 2 mm to achieve adequate absorption. Increased Hg concentrations are very desirable for the optimum collinear mode detector operation.

F.   Some Studies of the Collinear Mode

In the first phase of study of the collinear mode, some detectors with transparent contacts were made and the normal and collinear mode performances were compared. Groups of four detectors, all having transparent contacts, were arranged on a mounting block as shown in Figure 23. In this configuration the spectral response and time constant measurements of the two forms can be immediately compared.

46

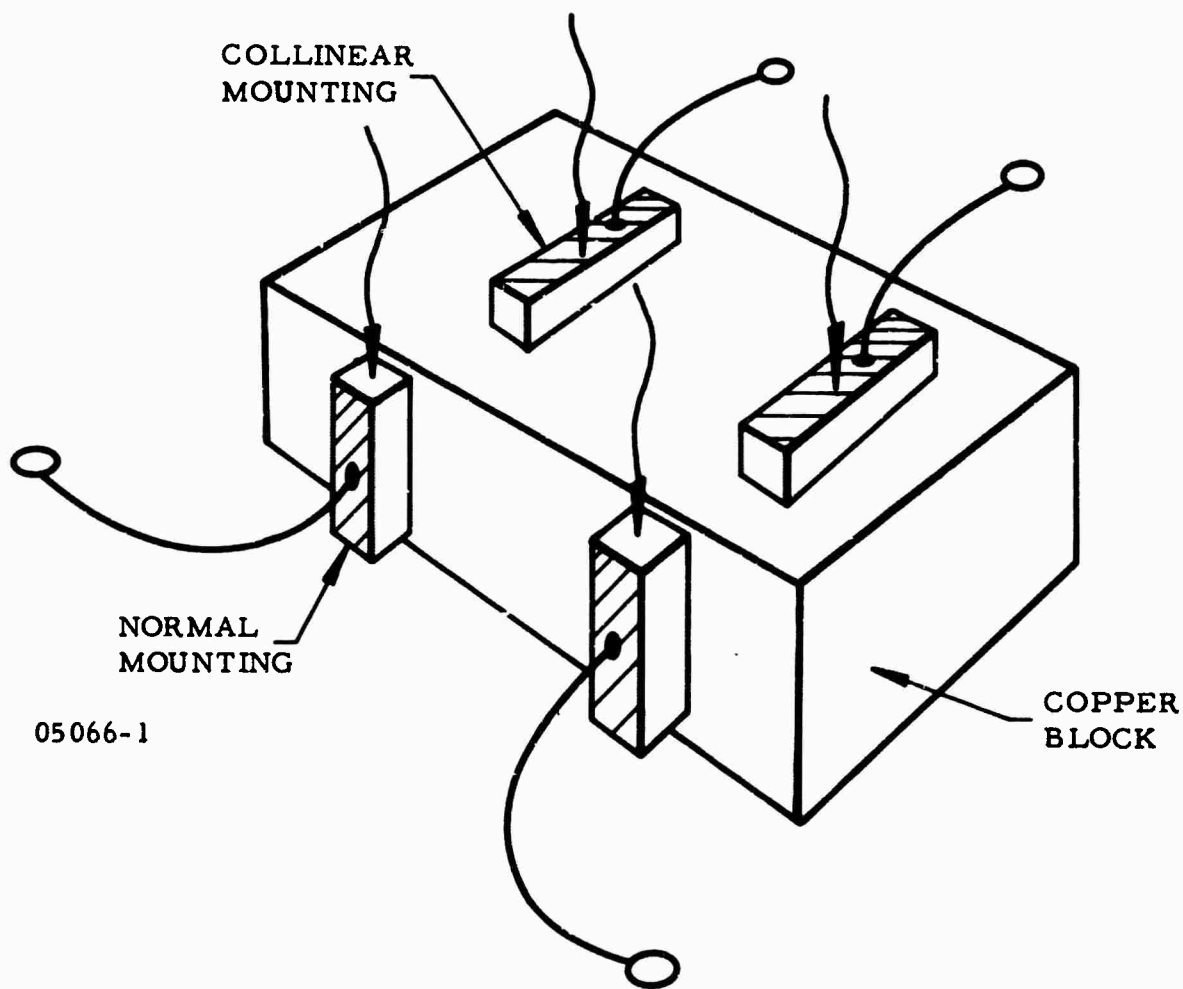COLLINEAR MOUNTING

NORMAL MOUNTING

05066-1

COPPER BLOCK

Figure 23   Arrangement of Detectors with Transparent Contacts to Permit Investigation of Normal and Collinear Modes of Operation During the Same Experimental Run

Figure 24 shows the spectral response of the two modes of operation utilizing a gold-gallium alloy contact, and Figure 25 shows spectral response for gallium diffused layers. It is apparent that no major difference occurs in the spectral response for the two modes of operation.

The long wavelength region has been emphasized, since recent work has demonstrated that spectral response in this region can be related to secondary effects within the detector.[11]

Radiation losses occurring as the signal passes through the Au-Ga contact have been determined by comparing the current responsivity for the normal and collinear modes. Data taken on several samples are collected in Table II. The following features are apparent. The collinear mode $\Delta I/I$ values are always larger than the normal mode values. Characteristics obtained with the set of Ge:Cu detectors having a gallium diffused layer were similar to those of the Ge:Hg samples and a Au-Ga alloy layer. Detector resistances were identical, to measurement accuracies, and thus are not listed separately. This is taken to indicate that a significant fraction of the 300°K background radiation reached the elements through surfaces other than the one facing the entrance aperture.

The normal and collinear detector elements had identical geometries; the mounting orientation determined whether the units were operated in the collinear or the normal mode (see Figure 23). Since the radiation absorbed will be largest in the first millimeter of the detector element, the collinear mode signal will be largest unless absorption in the contact layer reduces the signal. Thus, the average value of normal/collinear = 1.4 indicates a loss of at least 30% in the contact.

Contact resistance values were determined by measuring the resistance across two small contact points approximately 4 mm apart. Resistance values were approximately 7 ohms near 10°K.

The collinear and normal modes were compared in Section I.C. of the report, but no significant differences in operating characteristics have been noted.

48
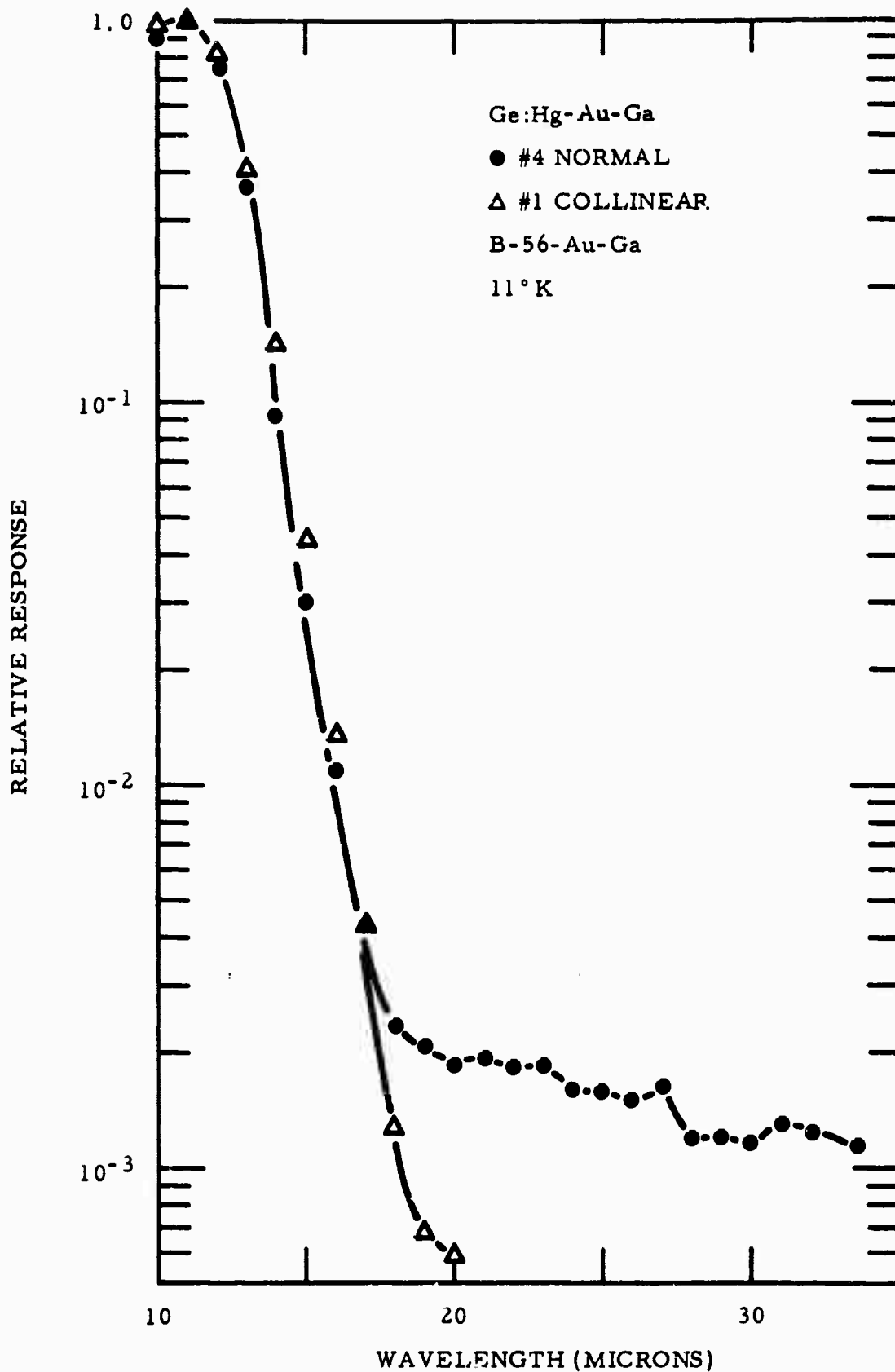
Figure 24   Normal and Collinear Spectral Response for a Gold-Gallium
Alloy Contact

49
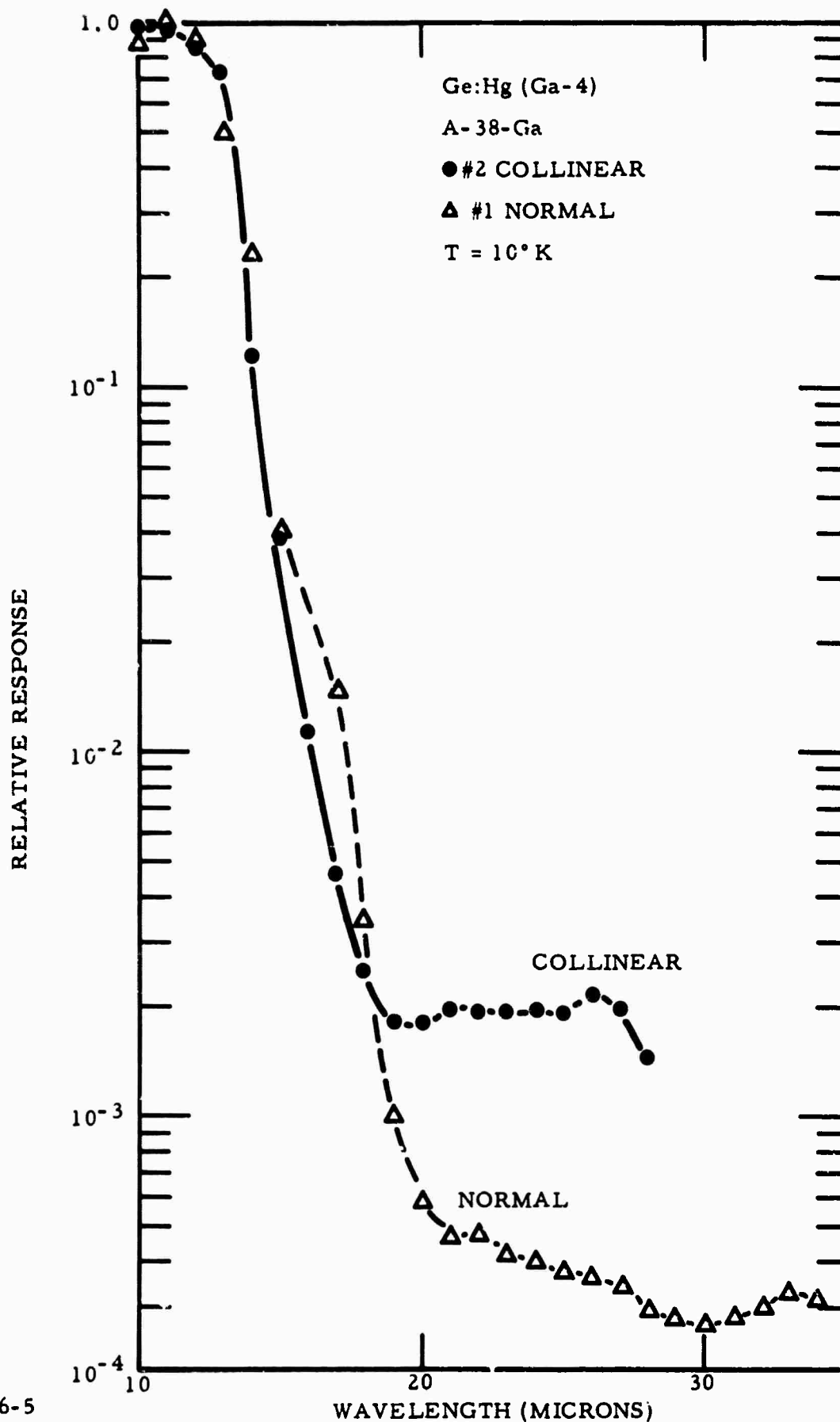
Figure 25   Normal and Collinear Spectral Response for a Gallium-Diffused Layer Contact

TABLE II

Collinear and Normal Detector Response in a Signal Field of 1.2×10^{-5} Watt/Cm^2

Crystal	Element Resistance	$\frac{\Delta I}{I} \times 10^4$				
		Normal		Collinear		Normal/
		actual	average	actual	average	Collinear
Au-Ga Alloy (Ge:Hg)						
DB 1170	0.4 MΩ	0.32		0.24		
		0.32		0.22		
			0.32		0.23	1.4
4-4-B-56	10 kΩ	0.49		0.36		
		0.46		0.28		
			0.48		0.32	1.5
7-1-A-56	18 kΩ	0.67		0.56		
		0.71		0.53		
			0.69		0.55	1.3
Ga Diffusion (Ge:Cu)						
Ge:Cu-4	130 kΩ	1.2		1.1		
				0.98		
			1.2		1.0	1.2
					Average $\frac{N}{C}$ = 1.4	

G. Alignment Requirements for Heterodyning

The discussion of heterodyning in this report assumed that the local oscillator signal and the incoming signal are perfectly aligned. Ross[12] gives an expression for the falloff of signal with misalignment angle θ as follows:

$$\frac{\text{Signal for } \theta = \theta}{\text{Signal for } \theta = 0} = phi = \frac{\sin(\beta\ell/2)}{(\beta\ell/2)} \quad,$$

where $\beta = 2\pi/\lambda_r \sin \theta$. In this expression λ_r is the wavelength of the radiation and ℓ is the dimension of the detector employed.

This expression was computer-calculated and is plotted in Figure 26. The data are for 10.6 micron radiation falling on detectors of varying dimensions ℓ. The situation described here is depicted in the insert of the figure. Note the critical angular tolerance; for a 1 mm detector the 50% falloff point is 0.36°. The alignment criterion is very severe for large detectors, indicating a practical necessity to use small detectors.
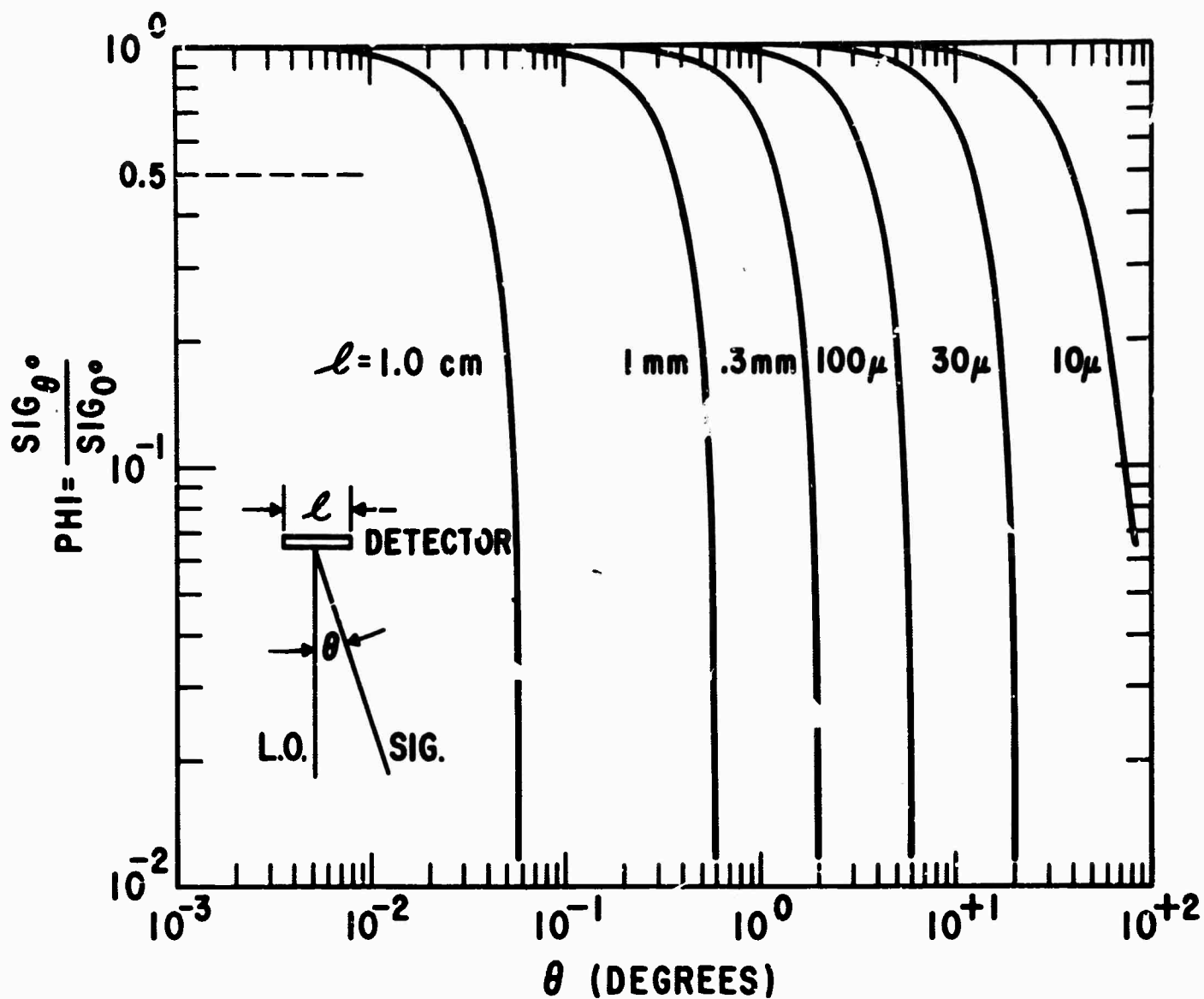
Figure 26 Fall-off in Signal Response with Angular Misalignment of Signal
and Local Oscillator Propagation Directions. The calculated
curves are for 10.6 micron radiation and various one-dimensional
detector dimensions given by each curve.

53

SECTION V

CONCLUSIONS AND RECOMMENDATIONS

It has been demonstrated that dielectric relaxation effects limit the speed
of response of extrinsic 0.1 eV detectors and that the maximum speed is determined
by the background photon flux. A review of gain, speed, and sensitivity to be
realized with extrinsic detectors revealed that substantial advantage can be
achieved using p-i-n diodes of intrinsic 0.1 eV material.

In view of the above conclusions, it is recommended that the continuation
of this work deal with fabrication of diodes as high speed 0.1 eV radiation detectors
utilizing HgCdTe and PbSnTe.

REFERENCES

1. F. M. Klaassen, K. M. van Vliet and J. R. Fassett, J. Phys. Chem. Solids 22, 391 (1962).

2. K. M. van Vliet and J. R. Fassett, in Fluctuation Phenomena in Solids, ed. by R. E. Burgess, (Academic Press, New York, 1965), Chapter V.

3. R. L. Williams, J. Appl. Phys. 38, 4802 (1967).

4. R. A. Reynolds, G. R. Cronin, W. G. Hutchinson, and R. A. Chapman, "Mercury Doped Germanium Study Program," Final Technical Report No. AFAL-TR-66-336 for Contr... AF 33(615)-3353, November 1966.

5. M. C. Teich, R. J. Keyes, and R. H. Kingston, Appl. Phys. Letters 9, 357 (1966).

6. C. S. Bucjek and G. S. Picus, Appl. Phys. Letters 11, 125 (1967).

7. M. C. Teich, Proc. IEEE 56, 37 (1968).

8. R. N. Hall and J. H. Racette, J. Appl. Phys. 35, 379 (1964).

9. G. B. Larabee and J. F. Osborne, J. Electrochem. Soc. 113, 564 (1966).

10. K. Weiser, M. Draugard, and R. Fern, J. Phys. Chem. Solids 28, 171 (1967).

11. R. L. Williams and B. H. Breazeale, Phys. Rev. Letters 25, 1129 (1967).

12. M. Ross, Laser Receivers (John Wiley and Sons, New York, 1966).

BLANK PAGE

DOCUMENT CONTROL DATA - R&D

(Security classification of title, body of abstract and indexing annotation must be entered when the overall report is classified)

1. ORIGINATING ACTIVITY *(Corporate author)*	2a. REPORT SECURITY CLASSIFICATION
Texas Instruments Incorporated 13500 North Central Expressway Dallas, Texas 75222	UNCLASSIFIED
	2b. GROUP

3. REPORT TITLE

HIGH-SPEED, LONG-WAVELENGTH COHERENT RADIATION DETECTORS

4. DESCRIPTIVE NOTES *(Type of report and inclusive dates)*

Final Technical Report, 15 May 1967 - 14 May 1968

5. AUTHOR(S) *(Last name, first name, initial)*

Williams, Robert L.

6. REPORT DATE	7a. TOTAL NO. OF PAGES	7b. NO. OF REFS
June 1968	54	12

8a. CONTRACT OR GRANT NO.	9a. ORIGINATOR'S REPORT NUMBER(S)
N00014-67-C-0497 b. PROJECT NO.	08-68-38
c. ARPA Order No. 269, Amend. No. 13	9b. OTHER REPORT NO(S) *(Any other numbers that may be assigned this report)*
d. Program Code No. 7E30	

10. AVAILABILITY/LIMITATION NOTICES

Reproduction in whole or in part is permitted for any purpose of the United States Government.

11. SUPPLEMENTARY NOTES	12. SPONSORING MILITARY ACTIVITY
	Office of Naval Research, Washington, D.C., in cooperation with Advanced Research Projects Agency, Washington, D. C.

13. ABSTRACT The four major sections of this report are concerned with four main areas of research performed under Contract N00014-67-C-0497. The first section deals with the appearance of dielectric relaxation time constant components. These arise when the drift length of holes becomes comparable to the electrode separation, so that a significant fraction of the photogenerated holes is swept from the crystal. Under these conditions, which correspond to having the photoconductive gain of the order of or greater than unity, there is a maximum D^* bandwidth product. The second section is concerned with the D^* bandwidth calculation and also points up the superiority of p-i-n diode performance over that of photoconductors if speed in excess of 10^{-9} second is required at 10.6 microns.

In the third section gettering and contact effects are reported. It is shown that a gallium diffused layer getters copper from Ge:Hg. Using radioactive copper, we have demonstrated a very irregular distribution of copper in the vicinity of the diffusion profile. In addition, photovoltaic studies have revealed an expected potential distribution near the contact.

Some general considerations on heterodyne detection form the fourth section of the report. Serious inefficiencies arise with misalignment of the local oscillator beam on an intrinsic photoconductor. A collinear mode of operation is shown to eliminate this effect, and studies of transparent contacts are reported. Finally, the loss of signal for misalignment of local oscillator and signal beams has been calculated for a variety of detector sizes and 10.6 micron radiation.

DD FORM 1473 1 JAN 64

14. KEY WORDS	LINK A		LINK B		LINK C	
	ROLE	WT	ROLE	WT	ROLE	WT
Photoconductivity in Ge:Hg and Ge:Cu.						
Response times limited by dielectric relaxation.						
D^* bandwidth limitations.						
Responsivity changes with electric field.						
Field dependent carrier lifetime.						
Interaction of Cu and Ga in Ge:Hg.						
Conditions for heterodyne detection.						

INSTRUCTIONS

1. **ORIGINATING ACTIVITY:** Enter the name and address of the contractor, subcontractor, grantee, Department of Defense activity or other organization (corporate author) issuing the report.

2a. **REPORT SECURITY CLASSIFICATION:** Enter the overall security classification of the report. Indicate whether "Restricted Data" is included. Marking is to be in accordance with appropriate security regulations.

2b. **GROUP:** Automatic downgrading is specified in DoD Directive 5200.10 and Armed Forces Industrial Manual. Enter the group number. Also, when applicable, show that optional markings have been used for Group 3 and Group 4 as authorized.

3. **REPORT TITLE:** Enter the complete report title in all capital letters. Titles in all cases should be unclassified. If a meaningful title cannot be selected without classification, show title classification in all capitals in parenthesis immediately following the title.

4. **DESCRIPTIVE NOTES:** If appropriate, enter the type of report, e.g., interim, progress, summary, annual, or final. Give the inclusive dates when a specific reporting period is covered.

5. **AUTHOR(S):** Enter the name(s) of author(s) as shown on or in the report. Enter last name, first name, middle initial. If military, show rank and branch of service. The name of the principal author is an absolute minimum requirement.

6. **REPORT DATE:** Enter the date of the report as day, month, year; or month, year. If more than one date appears on the report, use date of publication.

7a. **TOTAL NUMBER OF PAGES:** The total page count should follow normal pagination procedures, i.e., enter the number of pages containing information.

7b. **NUMBER OF REFERENCES:** Enter the total number of references cited in the report.

8a. **CONTRACT OR GRANT NUMBER:** If appropriate, enter the applicable number of the contract or grant under which the report was written.

8b, 8c, & 8d. **PROJECT NUMBER:** Enter the appropriate military department identification, such as project number, subproject number, system numbers, task number, etc.

9a. **ORIGINATOR'S REPORT NUMBER(S):** Enter the official report number by which the document will be identified and controlled by the originating activity. This number must be unique to this report.

9b. **OTHER REPORT NUMBER(S):** If the report has been assigned any other report numbers (either by the originator or by the sponsor), also enter this number(s).

10. **AVAILABILITY/LIMITATION NOTICES:** Enter any limitations on further dissemination of the report, other than those imposed by security classification, using standard statements such as:

(1) "Qualified requesters may obtain copies of this report from DDC."

(2) "Foreign announcement and dissemination of this report by DDC is not authorized."

(3) "U. S. Government agencies may obtain copies of this report directly from DDC. Other qualified DDC users shall request through
_____ ."

(4) "U. S. military agencies may obtain copies of this report directly from DDC. Other qualified users shall request through
_____ ."

(5) "All distribution of this report is controlled. Qualified DDC users shall request through
_____ ."

If the report has been furnished to the Office of Technical Services, Department of Commerce, for sale to the public, indicate this fact and enter the price, if known.

11. **SUPPLEMENTARY NOTES:** Use for additional explanatory notes.

12. **SPONSORING MILITARY ACTIVITY:** Enter the name of the departmental project office or laboratory sponsoring (paying for) the research and development. Include address.

13. **ABSTRACT:** Enter an abstract giving a brief and factual summary of the document indicative of the report, even though it may also appear elsewhere in the body of the technical report. If additional space is required, a continuation sheet shall be attached.

It is highly desirable that the abstract of classified reports be unclassified. Each paragraph of the abstract shall end with an indication of the military security classification of the information in the paragraph, represented as (TS), (S), (C), or (U).

There is no limitation on the length of the abstract. However, the suggested length is from 150 to 225 words.

14. **KEY WORDS:** Key words are technically meaningful terms or short phrases that characterize a report and may be used as index entries for cataloging the report. Key words must be selected so that no security classification is required. Identifiers, such as equipment model designation, trade name, military project code name, geographic location, may be used as key words but will be followed by an indication of technical context. The assignment of links, rules, and weights is optional.